### Title

The Relationship between Chemical Flexibility and Nanoscale Charge Collection in Hybrid Halide Perovskites




### Journal

Advanced Functional Materials, 28(18)

### ISSN

1616-301X



### Authors

Luo, Yanqi
Aharon, Sigalit
Stuckelberger, Michael
et al.



### Publication Date

2018-05-01

### DOI

10.1002/adfm.201706995

Peer reviewed

WILEY-VCH

DOI: 10.1002/ ((please add manuscript number))
**Article type:** Review

# The Relationship Between Chemical Flexibility and Nanoscale Charge Collection in Hybrid Halide Perovskites

*Yanqi Luo,[1] Sigalit Aharon,[2] Michael Stuckelberger,[3] Ernesto Magana,[1] Barry Lai,[4] Mariana I. Bertoni,[3] Lioz Etgar,[2] and David P. Fenning*[*,1]*

[1] Department of Nanoengineering, University of California San Diego, La Jolla, CA 92093. *dfenning@eng.ucsd.edu
[2] Institute of Chemistry, The Hebrew University of Jerusalem, Jerusalem, Israel, 91904
[3] School of Electrical, Computer and Energy Engineering, Arizona State University, Tempe, Arizona 85287
[4] Advanced Photon Source, Argonne National Laboratory, Argonne, IL 60439

Keywords: Hybrid perovskite, mixed halide, nanoprobe x-ray fluorescence

Hybrid organometal halide perovskites are known for their excellent optoelectronic functionality as well as their wide-ranging chemical flexibility. The composition of hybrid perovskite devices has trended toward increasing complexity as fine-tuned properties are pursued, including multi-element mixing on the constituent A, B, and halide sites. However, this tunability presents potential challenges for charge extraction in functional devices. Poor consistency and repeatability between devices may arise due to variations in composition and microstructure. Within a single device, spatial heterogeneity in composition and phase segregation may limit the device from achieving its performance potential. This article details how the nanoscale elemental distribution and charge collection in hybrid perovskite materials evolve as chemical complexity increases, highlighting recent results using non-destructive *operando* synchrotron-based X-ray nanoprobe techniques. The results reveal a strong link between local chemistry and charge collection that must be controlled to develop robust, high-performance hybrid perovskite materials for optoelectronic devices.

## 1. Introduction

Hybrid organic-inorganic perovskite materials have attracted increasing attention in the field of optoelectronic materials in the past decade, due to their great potential in a wide range of applications including solar cells,[1,2] light-emitting diodes,[3] lasers[4] and photodetectors.[5] The exceptional minority carrier diffusion lengths in these materials[6,7] leads to nearly 100% internal quantum efficiency[8] results in high charge carrier collection efficiency and high external luminescence efficiency in electron-photon conversion devices.[9] Particularly in the field of photovoltaics (PV), their extraordinary material properties[10–12] have enabled perovskite solar absorbers to achieve large improvements in device performance in the past 8 years. The perovskite crystal structure is shown in Figure 1a, where the A-site is $CH_3NH_3^+$ (MA, methylammonium), the B-site is $Pb^{2+}$, and the X-site is $I^-$ following the general perovskite formula $ABX_3$. After demonstration of a device with 3.8% power conversion efficiency (PCE) by Miyasaka and colleagues in a dye-sensitized solar cell architecture using $CH_3NH_3PbI_3$,[13] a breakthrough in perovskite photovoltaics occurred in 2012 when the first all-solid-state hybrid perovskite devices were shown by Kim *et al.*,[14] improving the chemical stability of the perovskite and enabling device performance to exceed beyond 9% using $CH_3NH_3PbI_3$ perovskites. With intense investigation of perovskite material properties from research groups all over the world, including bandgap engineering by halide mixing[15,16] and device optimization using A-site mixing,[9,17] the record PCE of hybrid perovskite solar cells reached 22.7% in 2017 after achieving 22.1% PCE in 2015[18] using mixture of formamidinium lead iodide ($CH(NH_2)_2PbI_3$) with 5% loading of methylammonium lead bromide ($CH_3NH_3PbBr_3$) chemistry.[19,20] Surpassing 22% PCE by leveraging the chemical flexibility of the perovskite structure brought hybrid perovskite solar cells on par in efficiency with most polycrystalline solar absorbers to date, exceeded only by single-crystal silicon and III-V technologies.

To fully exploit the hybrid perovskites for optoelectronic applications, robust functional thin films must be reproducibly realized. Their electronic and chemical instability due to

anomalous electronic hysteresis,[21] rapid decomposition under exposure to thermal,[22] UV or visible light,[23] and moisture[24] presents a critical challenge to the application of hybrid perovskites for optoelectronics.[25–27] The chemical flexibility of the perovskite once again holds promise to address these issues through substitution and control over the dimensionality of the perovskite[28] as it did for raising the performance of perovskite absorbers.

However, the chemical flexibility can also lead to new challenges. For example, the rapid progress in functional performance in mixed Br and I perovskites also revealed a new mechanism of instability under illumination,[23] which required stabilization by the further addition of inorganic A-site cations.[17] Of course, each of these chemical changes impacts the optoelectronic properties of hybrid perovskite devices as well. It is crucial to establish a foundational understanding of the perovskite film chemistry in final devices, how it varies in the three dimensions of the film, and how these variations relate to charge collection and mechanisms that may cause short operating lifetimes in hybrid perovskite devices. Because of the sub-micron thickness and grain sizes typically from hundreds of nanometers to few microns, nanoscale probes are required to effectively assess the heterogeneity in elemental composition at the scale relevant for device operation. Measurements of intragranular variations, of variations between grain boundaries and the bulk, and across the cross section of the device provide direct insight toward understanding device limitations and directions to improve the optoelectronic properties.

The purpose of this article is to provide an overview of how substitutions within the perovskite structure alter the local compositional heterogeneity within perovskite thin films and how this heterogeneity affects charge collection. We begin by reviewing the origins of chemical flexibility within the perovskite structure and examining the evolution of perovskite chemistry as it relates to solar cell device performance. Turning to focus on how the local chemistry at the nanoscale affects devices, we discuss various characterization tools for accessing this nanoscale information in the degradation-prone perovskite materials. Focusing on recent results from X-

ray microscopy, we discuss the role of local variations in chemistry on charge collection in perovskite materials of increasing chemical complexity, progressing from effects seen in single halide to mixed halide materials and finally to mixed A-site, mixed halide chemistries. The microscopic investigations reveal a critical link between the local chemistry within perovskite thin films and charge collection that must be controlled to develop robust, high-performance hybrid perovskite materials for optoelectronic devices.

## 2. Chemical Flexibility of Hybrid Perovskites: A Large Design Space to Tune Functional Properties

Hybrid perovskites are a broad family of inorganic-organic compounds that expand the material design space in the familiar $ABX_3$ perovskite crystal structure,[29] which includes the widely-studied inorganic oxide perovskites $ABO_3$.[30,31] The primitive crystal structure of the most studied hybrid lead halide perovskite today, methylammonium lead iodide $CH_3NH_3PbI_3$, is shown in Figure 1a, where A-site cation, B-site cation and X-site anion, are $CH_3NH_3^-$, $Pb^{2+}$, and $I^-$, respectively. Here we discuss the evolution in chemical composition of hybrid perovskite optoelectronic materials from $CH_3NH_3PbI_3$, trending away from single cation (A-site) and halide (X-site) chemistry to triple/quadruple cations and mixed halide composition to enhance device performance and long term operational and environmental stability.[9,13,17,32,33]

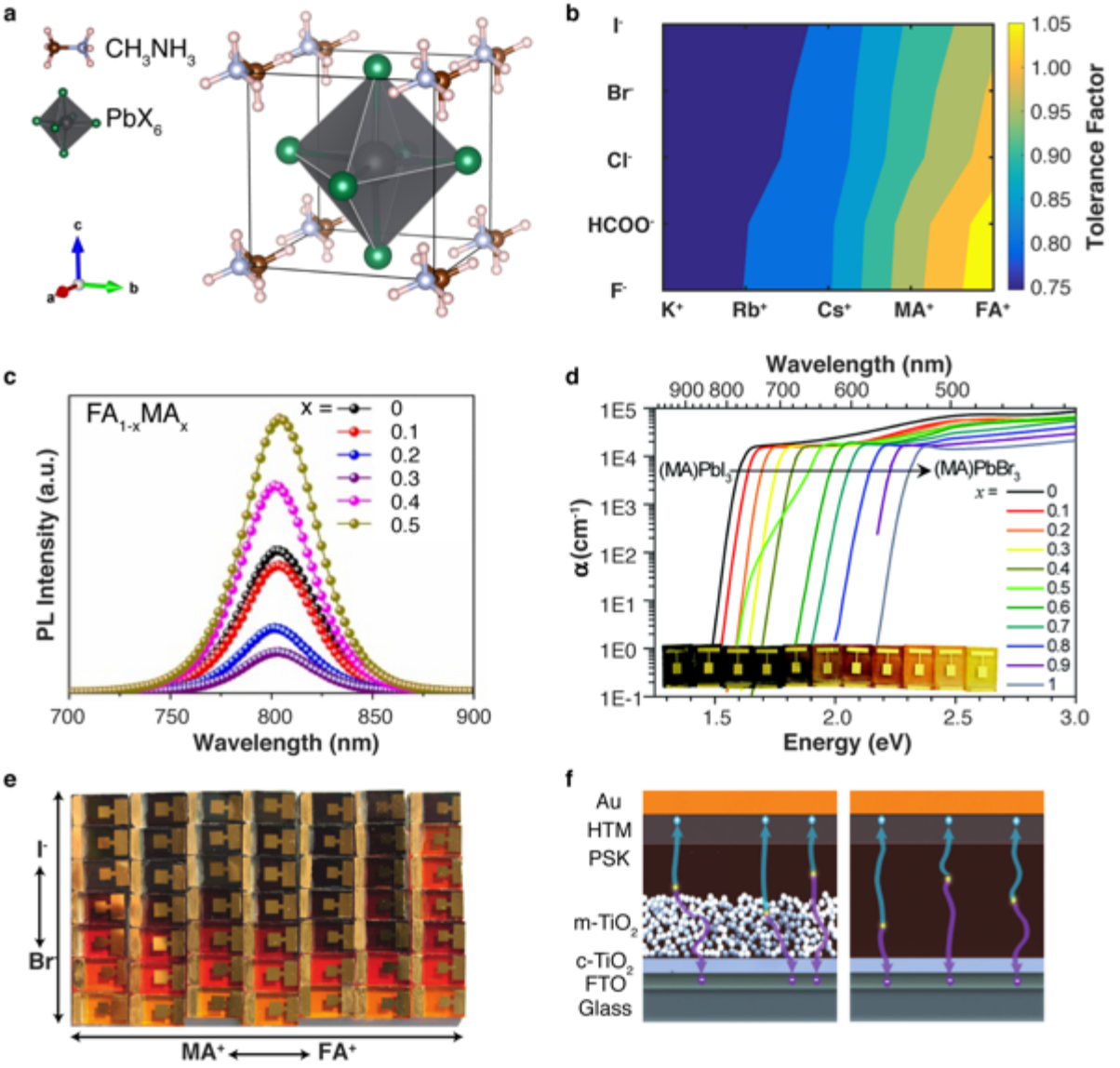


**Figure 1.** Hybrid organic-inorganic perovskite chemical flexibility and device structure. (a) A cubic unit cell of a hybrid methylammonium lead halide perovskite, with general $ABX_3$ chemical formula. (b) A contour plot of calculated non-modified Goldschmidt's tolerance factor for a range of hybrid perovskites using Shannon's ionic radii,[34] including A-site cations from $K^+$ to formamidinium ($FA^+$) and X-site anion from $F^-$ to $I^-$. (c) The photoluminescence spectra for triiodide mixed A-site cation perovskites shows little change in bandgap when varying MA/FA content. (d) The absorption spectra for MA-based perovskites of varying Br and I content show clear bandgap tunability. (e) Optical images of hybrid lead perovskites solar cells of 49 different chemistry compositions in the MA/FA and Br/I compositional space. (f) Schematic diagrams of typical perovskite solar cell layers using a glass superstrate, fluorine-doped tin oxide (FTO) transparent electrode, $TiO_2$ electron transport layer, perovskite absorber (PSK), hole transport material (HTM), and Au back contact in mesoporous (left) and planar (right) architectures. (c) Adapted with permission.[35] Copyright 2017, Elsevier. (d) Reproduced with permission. [23] Copyright 2015, Royal Society of Chemistry. (e) Adapted with permission.[36] Copyright 2016, Royal Society of Chemistry. (f) Adapted with permission. [25] Copyright 2015, Nature Nanotechnology.

Hybrid perovskite materials combine functional advantages of both inorganic and organic semiconducting materials. The introduction of an organic cation on the A-site to create the hybrid organic-inorganic material may contribute to unusual defect-tolerance[37] that facilitates minority carrier device functionality. As compared to organic semiconducting films, the charge transport mechanism in hybrid perovskite does not purely rely on overlapped π-orbitals between adjacent molecules[38] but rather depends on charge-carrier separation at the conduction and valence band edges as in inorganic materials. The inorganic framework of $PbI_6$ octahedra is formed due to strong lead-halide ionic interaction; and the electronic structure of perovskite is mainly constituted via this interaction, where the valance band is composed of Pb (6s orbital) and I (5p orbital) anti-bonding states, while the conduction band is attributed mainly to anti-bonding states of Pb (6p orbital) and I (5p orbital) interaction.[39,40] Optoelectronic investigations have focused on semiconducting lead halide perovskites, though extensive previous work in metallic stannous halide perovskites highlighted their exceptional electronic properties.[41,42] Recently, lead-tin alloys have also been pursed to reduce the bandgap toward optimal terrestrial values.[43–45] We focus here on the lead halide perovskites, given the explosive growth in recent work on their optoelectronic functionality.

Goldschmidt's tolerance factor has been demonstrated to be a valuable approach for evaluating the formability of existing and as-yet-undemonstrated perovskite compositions. In 1926, Goldschmidt developed the tolerance factor to estimate whether a specific elemental composition can exist within the perovskite structure on the basis of elemental ionic radii and crystal geometry.[46] As the hybrid perovskite material systems attracts increased attention, it encourages scholars to investigate undiscovered perovskite materials that may have potential to be excellent electronic, magnetic, or optical materials. Recently, Kieslich *et al.* calculated the ionic tolerance factor for over 2300 amine-metal-ion permutations, indicating roughly 742 compositions would adopt the perovskite structure.[47,48] Within these compositions, one seventh are known to be suitable for electronic applications.[47] The octahedral factor, derived

from the radius ratio rules of Pauling,[49] provides an additional easily-calculated and *necessary* criterion for the formability of halide perovskites.[50] Though formability is necessary, it is not sufficient for functional applications – reasonable thermodynamic stability is required. Density functional theory calculations can provide critical insight into the phase stability of predicted perovskite phases to identify promising candidates for experimental demonstration and testing.[51]

Tolerance factor calculations provide a framework to understand the current landscape of hybrid perovskite compositions, and they illustrate the chemical flexibility of perovskites. **Figure 1b** displays a contour plot of tolerance factor for $Pb^{2+}$ B-site cation perovskites using a non-modified Goldschmidt equation, covering wide range of A-site cations from $K^+$ to formamidinium (FA) ion and X-site anions from fluoride to iodide. The Shannon's ionic radii are used in the tolerance factor calculation.[34] The contours of the tolerance span 0.75 to 1.05, where the tolerance factor of photoactive black phase hybrid perovskite is commonly found within the range of 0.8 to 1.0.[9] The contours of the tolerance factor indicate the structural formability of the hybrid perovskite is dominated by the size of large A-site occupants in lead perovskites. However, the optical properties of the 3-dimensional (3D) hybrid lead perovskite do not show a strong dependence on different A-site ion composition, as shown in **Figure 1c** using photoluminescence (PL) data as an example.[35] PL emission centers around 800 nm for perovskite samples that have FA or mixture of FA and MA as the A-site cation.

Expanding beyond the 3D perovskite structure through the incorporation of larger A-site cations can vastly broaden the structural and functional design space of hybrid perovskites,[29] though the highest performing hybrid perovskite solar cells to date are the 3D perovskites. The dimensionality of the perovskites can be tuned from 2D[52,53] to Ruddlesden-Popper quasi-2D[54,55] to fully 3D perovskite structures by incorporating larger organic A-site molecules such as 2-phenylethylammonium (PEA) or *n*-butylammonium (*n*-BA).[56,57] In the 3D perovskite framework, the commonly used A-site cations (methylammonium or

formamidinium) reside in the cages formed by the corner sharing $PbX_6$ layer networks. In contrast, the 2D structure can be regarded as *n* number of octahedral perovskite layers sandwiched top and bottom by two layers of larger A-site organic cations. These large organic molecules, also known as organic spacers, prevent the continuous growth of perovskite 3D lattices resulting in a quasi-2D layered structure with a mixture of organic spacers and perovskite domains. The addition of the longer-chained hydrophobic cations has been shown to offer greater environmental stability to the hybrid perovskite.[58] In addition to determining the perovskite dimensionality, the size of A-site cation plays an important role on $PbX_6$ octahedron tilting, which can influence the electronic structure of the materials indirectly.[29,59] In this contribution, we narrow our focus to the relationship between nanoscale chemistry and charge-collection properties of 3D hybrid perovskites as they have exhibited the highest performance in optoelectronic applications to date.

Substitution of different halide anions within the 3D perovskite structure, enables us to tune the perovskite materials' optoelectronic properties significantly as shown in **Figure 1d**. Changes to the lead halide bonding,[12] which contributes the valence and conduction band density of states, lead to sensitive changes in the functional capability of the perovskite.[10,11] Figure 1d displays the absorption coefficients of different halide film compositions upon substituting $I^-$ with $Br^-$.[23] The absorption wavelength of halide perovskites can be fine-tuned in the range of 800 nm to 520 nm by having the appropriate Br to I ratio. Both absorption and photoluminescence spectra clearly indicate the optoelectronic tunability that emerges from the structural flexibility of hybrid perovskites. In the early stage of the hybrid perovskite development, different halide compositions, ranging from single halide (Cl, Br, and I) to mixed halide Br/I,[23,60,61] were explored extensively while fixing the A-site cation for pursuing the better fine-tuned optoelectronic properties. Impressively, the structural flexibility extends to post-fabrication chemical modifications, including gas-solid heterogeneous reactions. For example, Solis-lbarra *et al*. found that $MAPbI_3$ perovskite films can undergo halide

conversion/exchange after exposure to $Br_2$ or $Cl_2$.[62] This observation indicates the structural flexibility of $MAPbI_3$ thin films but also suggests the instability of the material itself.[63,64]

Incorporation of a small but increasing Br fraction relative to I promotes better environmental stability for MA based perovskite devices.[65] The PCE of mixed halide $MAPbI_{3-x}Br_x$ devices, where x = 0.20 and 0.29, display almost no PCE decrease after storing for 20 days at 35% humidity, while the PCE of the triiodide system drops from 11.2% to 2.5%.[15] However, this mixed halide composition appears to have poor photostability upon laser/light illumination resulting in a shift in the PL peak from 635 nm to 730 nm[23] and formation of a secondary phase.[36]

To improve the long-term photo- and environmental stability in mixed Br/I phases, mixed A-site cations were introduced to the mixed halide hybrid perovskite. Remarkable advances have been achieved by precise compositional engineering. First, the addition of $MAPbBr_3$ to $FAPbI_3$ in small quantities has been demonstrated to produce better film coverage and stabilization of $FAPbI_3$ (nominally, outside the perovskite formability window, Figure 1b) achieving a PCE of 17.9% by Jeon *et al*. with $(FAPbI_3)_{0.85}(MAPbBr_3)_{0.15}$[66] and 22.1% by Yang *et al.* using an optimized $(FAPbI_3)_{0.95}(MAPbBr_3)_{0.05}$ with additional iodide ions in organic cation precursor solutions.[20] Optical photographs of 49 different devices with chemical compositions within the mixed A-site, mixed halide $MA_{1-x}FA_xPbI_{1-y}Br_y$ system are shown in **Figure 1e**. The composition space starts with $MAPbBr_3$ at the lower left, with increasing FA and I content, incremented by 1 part in 6 for each row and column on the abscissa and the ordinate axes, respectively, until the final composition of $FAPbI_3$ is reached in the top right corner. The color of the final thin film changes from orange to black color as I incorporation increases. In contrast, the film color appears quite similar at various MA:FA ratio at a specific Br or I concentration, except for the pure FA phases. The adjustable bandgap visualized here provides the ability to fabricate a wide-range of optoelectronic devices, including bandgap-tunable perovskite-perovskite tandem solar cells.[67]

Later, inorganic A-site cations were introduced into these complex mixed A-site, mixed halide perovskites, imparting improved stability. Inorganic $CsPbBr_3$ perovskites exhibit excellent thermal and phase stability up to 600°C, offering promise for LEDs and other optoelectronics, though their bandgap (2.25 eV) is non-ideal for PV applications.[17,68,69] Choi *et al.* demonstrated Cs incorporation in $MAPbI_3$, creating mixed Cs/MA lead iodide perovskites, resulting in stable perovskite films reaching to 7.68 % PCE.[70] The Cs/FA lead iodide compositional space was explored by Lee *et al*, who found that substituting a small amount of Cs helps to not only stabilize the photoactive black phase of $FAPbI_3$ but also improve the PCE from 16.3% to 17.1 %.[71] The presence of Cs and its effect on $FAPbI_3$ phase stabilization can be understood on the basis of entropic stabilization and the Goldschmidt tolerance factor.[72,73] The mixed Cs/FA cation chemistry exhibits significantly improved environmental stability with respect to $FAPbI_3$, maintaining 70 % of the initial device performance after 220 hours of continuous light exposure while the pure FA cation lead iodide perovskites do not operate after 70 hours in the same testing conditions. [71]

These promising mixed inorganic-organic A-site investigations motivated novel hybrid perovskite chemistries combining triple A-site cations ($Cs^+$, $MA^+$ and $FA^+$) and mixed halides. Saliba *et al*. achieved 21.2% efficiency that was maintained over 250 hours under constant illumination at room temperature in a nitrogen atmosphere.[17] Expanding the design space further, Saliba *et al*. incorporated a fourth A-site cation in small quantities, $Rb^+$, in quadruple cation ($Rb^+$, $Cs^+$, $MA^+$ and $FA^+$) mixed A-site Br/I halide perovskites, yielding chemistry of $Rb_{0.05}(Cs_{0.05}(MA_{0.17}FA_{0.83})_{0.95})_{0.95}Pb(I_{0.83}Br_{0.17})_3$, to achieve yet higher photovoltaic performance of 21.6%, improved reproducibility, and further improved stability.[9] With rapid advances in the chemical complexity of hybrid perovskite materials, how mixing organic and inorganic rubidium/cesium cations on the A-site and halide mixing of the X-site impact charge collection at the nanoscale have remained open questions.

Before turning to how the modifications in perovskite chemistry described above affect charge collection, it is informative to briefly review the typical perovskite device structure to understand where charge extraction occurs. Hybrid perovskite solar cells are generally assembled in a simple heterostructure-like architecture**.** Usually, the active perovskite absorber is sandwiched between the top electron transport layer (ETL) and hole transport layer (HTL), yielding a layered architecture of top contact/ETL/perovskite (PSK)/HTL/back contact (**Figure 1f**). Cross-sectional electron beam induced current measurements of such $MAPbI_{3-x}Cl_x$ cells revealed that the heterostructure behaves as a *n-i-p* structure,[74] with charge separating junctions at both carrier selective contacts and a high quality intrinsic absorber between. $MAPbBr_3$-based devices in the same architecture exhibit only a *p-n* junction at the electron selective contact and hole-transport layer free MAPbBr3 cells have achieved high voltage (1.11 V),[75] highlighting the importance of the perovskite-ETL interface. Mesoporous $TiO_2$ and planar $SnO_2$ layers are broadly used as effective ETLs. Most commonly, a mesoporous $TiO_2$ layer is used as the ETL,[65,76] which allows the perovskite absorber to infiltrate the voids between $TiO_2$ nanoparticles, enhancing adhesion to the electron selective contact and improving charge extraction. Most perovskite devices with PCE above 20% report a mesoporous $TiO_2$ layer.[9,77] However, a planar $TiO_2$ layer without the meso- or nano-particles can also provide a moderate 12-15% efficiency with either solution or vapor deposited perovskite absorber.[78,79] The other principal alternative for ETL is planar $SnO_2$, which has shown promising device performance above 20% efficiency.[80–82] $SnO_x$ layers processed at low temperatures have shown better band edge alignment with perovskites layer and effective hole blocking ability.[83,84] The $SnO_x$ planar structure and morphology largely reduces the interface complexity and lowers the variability by reducing the impact of the $TiO_2$ nanoparticles on final absorber morphology.[85,86] Given the importance of this interface, a number of recent studies have focused on interface engineering and electron mobility enhancement in the selective contacts.[84,87] Below, we focus on X-ray nanoprobe studies using $TiO_2$ ETLs to isolate the

effect of the absorber chemistry on charge collection. Given the increase complexity of hybrid perovskite active materials and their complicated sensitivity to environmental conditions, it is critical to establish approaches to understand chemical heterogeneity within perovskite thin films and its role in determining the functional properties of devices.[1]

### 3. Tools to Assess Nanoscale Perovskite Chemistry and Its Optoelectronic Impacts

Focused visible light lasers, scanning probes, electron beams, and X-ray beams each offer unique advantages toward understanding the nanoscale optoelectronic quality in perovskite materials and devices. We have highlighted a cross-section of some of the most applicable tools researchers are using to characterize perovskite materials on the nanoscale, dividing them into tools that characterize optoelectronic properties, chemical properties, and the relatively few techniques or platforms that can provide a combination of both in **Figure 2**.

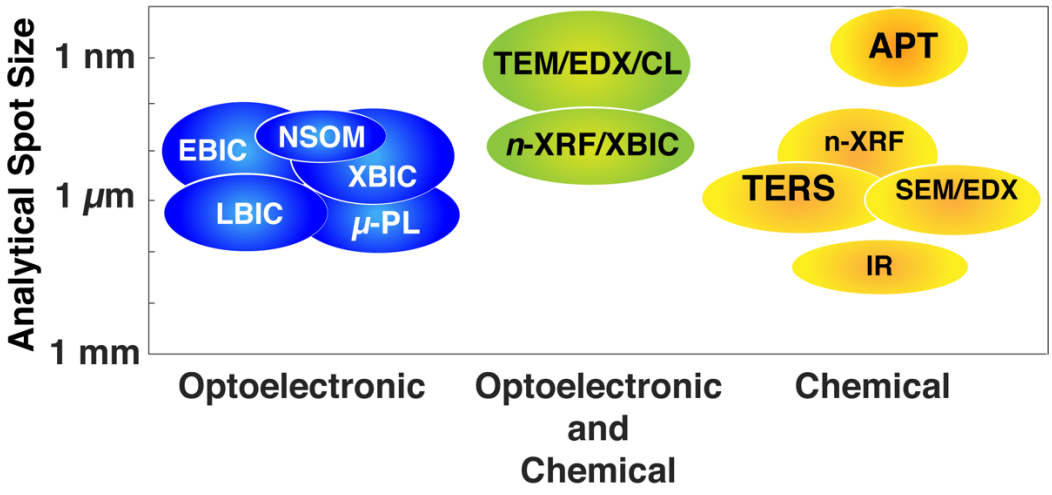


**Figure 2.** Optoelectronic and chemical characterization techniques and their analytical spot size. Five techniques, near-field scanning optical microscope (NSOM), electron beam induced current (EBIC), X-ray beam induced current (XBIC), Laser beam induced current (LBIC) and micro-photoluminescence (μ-PL) are grouped in blue as techniques that access optoelectronic insights. Atomic probe tomography (APT), nano-Xray fluorescence (n-XRF), tip-enhanced Raman spectroscopy (TERS), energy dispersive X-ray spectroscopy (EDX) and IR spectroscopy are characterization tools that collect elemental and chemical bonding information. The in-situ techniques for collecting both chemical and optoelectronic properties are shown in green ovals, which highlight transmission electron microscopy (TEM) based EDX and cathodoluminescence (CL) and n-XRF/XBIC.

Regarding characterization approaches to quantify nanoscale optoelectronic properties, we focus on summarizing the advantage and limitations of spatially resolved photoluminescence mapping (μ-PL), scanning probe microscopy, laser-beam induced current (LBIC), electron-beam induced current (EBIC) and energy-dispersive spectroscopy, and finally synchrotron-based X-ray fluorescence and x-ray beam induced current (XBIC). We discuss tradeoffs and the insights brought by these techniques to the rapidly growing hybrid perovskite field.

The quality of perovskite materials is often evaluated prior to the device stage by steady-state or time-resolved photoluminescence. Less frequently, current-voltage and EQE measurements on the device level are supplemented by local assessment of charge collection via laser beam induced current measurements. Near-field scanning probes surpass the diffraction limitations of typical optical microscopy to reveal nanoscale photovoltage variations. Because of hybrid perovskite materials' relative instability and especially their sensitivity to radiation exposure or different environmental conditions, techniques that combine chemical and electronic characterization offer additional value, particularly for *in-situ* and *operando* measurement techniques to reveal and realize the nanoscale chemistry variations and their electronic impact in hybrid perovskites. Unlike typical optical methods, E-beam and X-ray platforms typically offer serial or simultaneous chemical composition mapping. Electron-beam induced current (EBIC) and X-ray beam induced current (XBIC) can extend LBIC functionality to the nanoscale, past the visible light diffraction limit, to assess the operating mechanism of photovoltaic devices, to detect and evaluate the impact of extend defects, and to understand the dynamics of charge-carrier collection at the end of photovoltaics fabrication process when both n- and p- type contacts are deposited.

### 3.1. Non-Contact Optoelectronic Micro-Characterization: μ-PL and Near-Field Approaches

The main advantage of μ-PL is that it does not require a complete solar cell nor electrical contacts, and the measurements are generally taken under easily-controlled ambient conditions rather than high vacuum. μ-PL mapping provides an often-qualitative measure of the local radiative recombination and the associated PL emission wavelength and is a critical tool for understanding the performance of perovskite materials in functional devices. deQuilettes *et al.* applied the μ-PL mapping technique on perovskite thin films with chemistry of $MAPbI_{3-x}Cl_x$ to reveal that PL intensity varies significantly between grains within the same sample.[1] The spatially resolved μ-PL mapping also indicated that carrier recombination was limiting collection from grain boundaries relative to the bulk, which was improved greatly by Lewis-base passivation.[88] In contrast, an irreparable inhomogenous PL distribution and low carrier lifetime are detected as a consequence of any $PbI_2$ aggregation or formation.[89,90] Beyond forensic analysis, μ-PL can also serve as a rapid screen for material exploration. *Quantitative* mapping of the absolute intensity photoluminescence as a function of position in a combinatorial deposition of mixed Br and I chemistries by Braly and Hillhouse[91] enabled high-throughput chemical screening by quantifying the quasi-fermi level splitting as shown in **Figure 3a**.

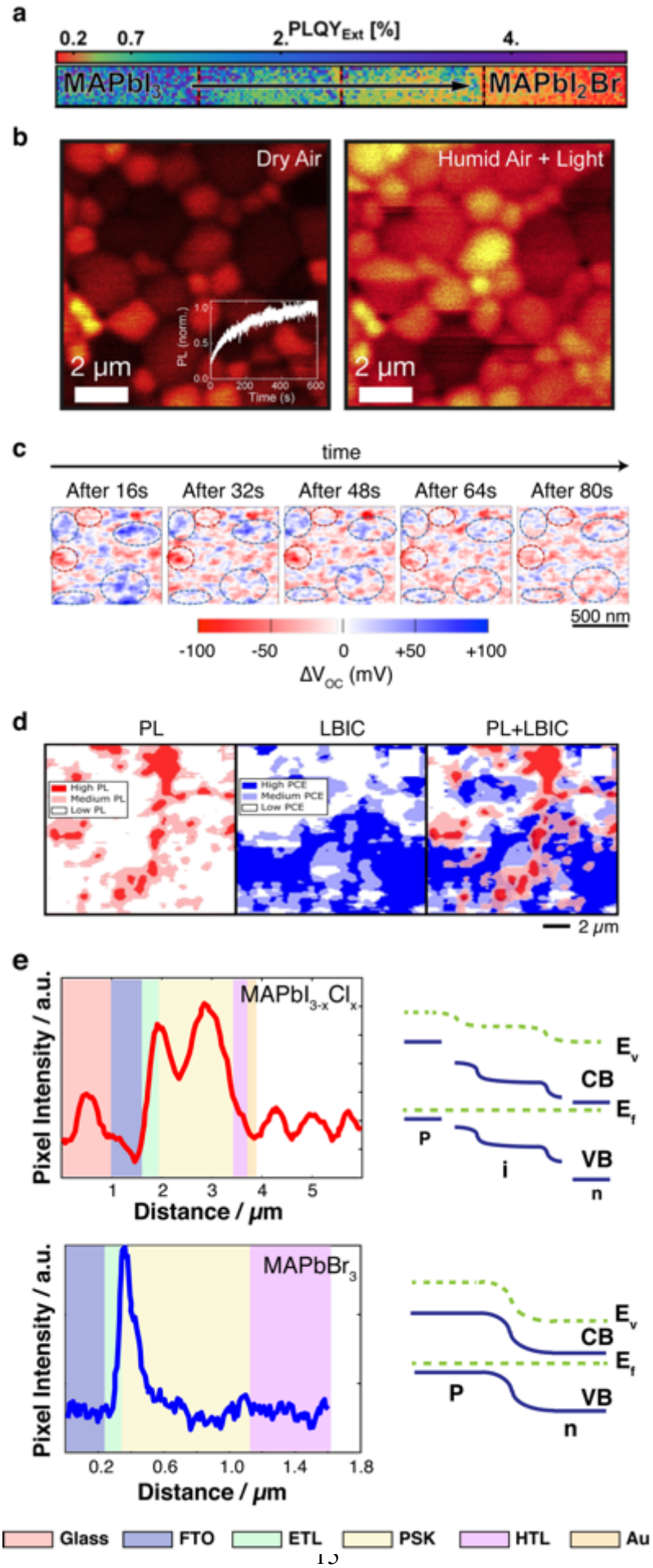
a
0.2
0.7
2.
4.
PLQY$_{Ext}$ [%]
MAPbI$_3$
MAPbI$_2$Br
b
Dry Air
Humid Air + Light
2 µm
2 µm
PL (norm.)
Time (s)
c
time
After 16s
After 32s
After 48s
After 64s
After 80s
500 nm
-100
-50
0
+50
+100
ΔV$_{OC}$ (mV)
d
PL
LBIC
PL+LBIC
High PL
Medium PL
Low PL
High PCE
Medium PCE
Low PCE
2 µm
e
Pixel Intensity / a.u.
MAPbI$_{3-x}$Cl$_x$
Distance / µm
E$_v$
CB
E$_f$
P
i
VB
n
MAPbBr$_3$
Glass
FTO
ETL
PSK
HTL
Au

**Figure 3.** Mechanistic insights are gained from nanoscale optoelectronic characterization of perovskite solar cells as a function of chemistry. (a) The photoluminescence quantum yield (PLQY) measurement of MA-based mixed halide Br/I perovskites where a Br gradient is established in the film spatially left to right. (b) μ-PL mapping of a $MAPbI_3$ film in dry air (left) and illuminated humid air (right) conditions, demonstrating significant surface passivation under humid, illuminated, oxygen-containing atmosphere.[91] (c) NSOM characterization reveals time dependent open circuit voltage and photocurrent dynamics of $MAPbI_3$ perovskites on the nanoscale. Blue areas shown relative $V_{oc}$ improvement under 500 nm irradiation while red areas degrade, with differences attributed to ion migration. (d) Segmented μ-PL, LBIC, and overlaid μ-PL/LBIC maps of a $MAPbI_3$ device. High, medium, and low PL areas are shown in dark red, light red, and white, respectively. High, medium, and low local efficiency areas are shown in dark blue, light blue, and white, respectively. The LBIC and μ-PL of the same film show an anti-correlated relationship between local photocurrent and photoluminesence within $MAPbI_3$ devices (e) EBIC studies in cross-section are used to examine charge separation mechanisms in $MAPbI_{3-x}Cl_x$ (top) and $MAPbBr_3$ (bottom). The $MAPbI_{3-x}Cl_x$ exhibits p-i-n behavior, with charge separation at both ETL and HTL junctions, while $MAPbBr_3$, devices adopt a p-n behavior with charge separating at the ETL interface, as shown schematically to the right. (a) Reproduced with permission. Copyright 2016, American Chemical Society.[91] (c) Reproduced with permission.[92] Copyright 2017, American Chemical Society. (d) Adapted with permission.[90] Copyright 2016, American Chemical Society. (e) Adapted with permission.[74,93] Copyright 2014, Macmillan Publishers Limited; and copyright 2015, American Chemical Society.

PL measurement is easily implemented in different environmental conditions for *in situ* study, which is critical for understanding the behavior of the dynamic perovskite materials. For both $MAPbBr_3$ and $MAPbI_3$ thin films and single crystals, PL is strongest when devices operate in regular air or oxygen-containing conditions, while weaker PL is found when nitrogen is introduced and little PL is detected when devices are under vacuum.[94–96] Exposure of $MAPbI_3$ films to oxygen, moisture, *and light* appears to create a semi-permanent surface passivation layer that improves the photoluminescence of perovskite thin films substantially, achieving 32 μs carrier lifetimes.[97] μ-PL mapping of a $MAPbI_3$ thin film in dry air and after illumination in humid air conditions is presented in **Figure 3**b. The enhanced PL in the presence of $O_2$ and light is attributed to a photochemical reaction at the thin film surface. Conversely, PL reduction under vacuum is suspected to be the consequence of desorption or de-bonding of passivating $H_2O$ and $O_2$-related species, resulting in higher carrier surface recombination velocity and higher density of defect states in hybrid perovskites.[96,98,99] The losses under vacuum conditions indicated by

PL were recently substantiated by the observation of reversible $V_{oc}$ loss under vacuum attributed to dehydration of $MAPbI_3$ with subsequent partial rehydration upon return to ambient conditions.[100]

At the frontier of high-resolution non-contact optoelectronic assessment, near-field scanning optical microscopy can provide multiple modes of optoelectronic information[101] at high resolution via mapping with as small as a 50 nm spot size, far beyond the diffraction limit of conventional optical microscopes.[102] Photoconductive atomic force microscopy has revealed nanoscale variations due to microstructure in photoresponse.[103] Recently, the time-dependent open circuit voltage and photocurrent dynamics of $MAPbI_3$ cells under light bias were monitored in real-time via NSOM shown in **Figure 3c**.[92] The scanning probe platform can also be extended into the infrared to gain access to local infrared vibrational spectroscopy, which can provide valuable insight regarding the behavior of the organic component of the hybrid perovskite.[104] For example, Yuan *et al.* showed that photovoltaic switching in lateral $MAPbI_3$ perovskite devices is related to the migration of the methylammonium cation using photothermal infrared microscopy. A valuable review of the application of scanning probe microscopy to halide perovskites was recently published.[105] NSOM and related optically-excited scanning probe microscopy techniques hold promise for gaining truly nanoscale insight into the operating mechanisms and *in situ* response of perovskite solar cells.

As generally practiced, photoluminescence is conducted under open-circuit conditions (or without any contacts present at all), while for an operating optoelectronic device we must either extract or inject current. To study charge extraction and injection, induced current measurements are especially useful.

### 3.2. Charge Collection Characterization via LBIC

LBIC is a powerful technique for correlating charge collection properties together with visible light or near-IR optical properties, even over large area cells. Spectrally-resolved LBIC

can be used to evaluate the relative collection of blue vs. near-infrared light, highly-relevant to the design of the front and back surfaces for 1-sun operation.[106] Its analytical spot size can be diffraction-limited but is usually in the micron to millimeter range, which is large compared to EBIC/XBIC nanoprobes. LBIC technique was first applied to characterize large area perovskite materials by Mastroianni *et al*,[107] while Song *et al* used LBIC to study the non-uniformity of photocurrent and degradation mechanism in water for the perovskite/Si tandem device.[108]

Perovskite materials show distinct behavior when probed under current-extraction conditions that does not directly follow from the open-circuit measurement of non-contact approaches. To better understand local heterogeneity within perovskite devices, high resolution spatially-resolved LBIC measurement conducted via an Au-coated AFM tip was recently compared against μ-PL by Eperon *et al*.[90] An anti-correlated relationship was found between local photocurrent and photoluminescence within $MAPbI_3$ chemistry with inverted architecture, shown in **Figure 3d**. From comparison between devices with and without the PCBM electron transport layer, the spatially-resolved characterization indicated that the heterogeneity originated in the perovskite materials itself and not in the contact layers. The authors suggest this anti-correlation may due to the excess $PbI_2$ aggregating at the poorly perform regions, as $PbI_2$ may form the insulating carrier extraction barrier. High-resolution μ-PL and LBIC characterization provides crucial optoelectronic insight, but chemical information is often required at similar scales to attribute the root cause of observed behavior.

### 3.3. Electrons as A Local Probe: Narrow Characterization Window for Hybrid Perovskites

Electron-microscope based energy dispersive X-ray spectroscopy (EDX) offers the potential for composition mapping, while the E-beam platform offers the opportunity to extract E-beam induced current (EBIC) to reveal nanoscale charge collection behavior. Electron beams interact strongly with matter, generating a characteristic pear-shaped interaction volume in

materials upon electron irradiation due to the cascade of secondary electron relaxations.[109] Characteristic X-rays are generated throughout the volume and can be sampled by an energy-dispersive or wavelength-dispersive spectroscopic detector.[110] Backscattered and secondary electrons from successively shallower depths provide familiar imaging modalities. A fraction of energetic electrons thermalizes completely to the band edges of the material. These excited carriers can then be collected as in an operating solar cell if the device is completed with contacts, and the E-beam induced current (EBIC) measured in plain view provides microscopic detection of defects or can examine the space charge region and charge separating properties of the junction in cross-section. The beam interaction volume can be tuned by adjusting the acceleration voltage to preferentially sample more surface vs. bulk electronic information.[111] Using EDX measurement, an E-beam 2 to 3 times higher in energy than critical electron binding energy of an atom is often necessary to obtain acceptable characteristic X-ray signal,[112] and the Brehmsstrahlung background radiation generally limits sensitivity to ~0.1%.[113] E-beam electronic characterization of hybrid perovskite materials is extremely difficult due to the material's beam sensitivity and fast degradation under even short exposure to electron irradiation.[114]

Despite these challenges, EDX has been used successfully to identify composition and investigate trace element distribution in hybrid perovskites. In the early stage of perovskite solar cell development, EDX was used to determine the perovskite layer thickness and its incorporation with the mesoporous $TiO_2$ nanoparticles by Lee *et al*.[115] Later, as incorporation of chlorine (Cl) containing precursors showed better grain growth,[116–118] EDX was used to investigate Cl incorporation in the final film but the data led to varying conclusions. Many studies failed to identify Cl incorporation from EDX characterization and concluded chlorine sublimes completely during the final device annealing step or the incorporated amount is below the detection limit of EDX.[117–119] Only a few EDX studies successfully detected the incorporation of chlorine in the final perovskites films.[1,120]

With carefully optimized E-beam parameters, rigorous cross-sectional EBIC study investigating the charge collection and transport dynamics within $MAPbI_{3-x}Cl_x$ and $MAPbBr_3$ was completed by Edri *et al.* and Kedem *et al*.[74,93,114] These two studies evidenced different carrier transport mechanism within perovskites with different halide substituents. The carrier generation line profiles are shown in **Figure 3e**. In the case of triiodide perovskites, the EBIC study provides direct evidence for the model of *p-i-n* junction within perovskite devices where the perovskite absorber is largely an intrinsic layer. The relative EBIC signal difference at the junction of the perovskite with the adjacent *p*- or *n*-type selective contacts indicates efficient charge extraction at these two interfaces. In contrast, $MAPbBr_3$ absorbers behave as a *p-n* junction, where charge extraction occurs mostly at the perovskite/n-type contact ($TiO_2$) interface and the rest of carrier transport pathway to the other type of contact relies heavily on diffusion after the space charged region. In both scenarios, carrier diffusion lengths can be estimated using cross-section EBIC measurement. The diffusion lengths for $MAPbI_3$ and $MAPbBr_3$ are calculated to be 1.5 and 0.4 μm, respectively, which agree with values estimated from TR-PL studies by Snaith *et al*.[79] Non-contact optoelectronic information can also be gained in electron microscope platforms via cathodoluminescence, the E-beam analog of photoluminescence. STEM-based cathodoluminescence was used by Hentz *et al*. to correlate iodide segregation and non-stoichiometry in $MAPbI_3$ with detrimental electronic impacts.[121] Critically, Edri *et al.*[122] and Hentz *et al*.[121] both study in detail the E-beam probe's effects on the perovskite material, establishing the necessary experimental foundation to extract meaningful information from EBIC characterization.

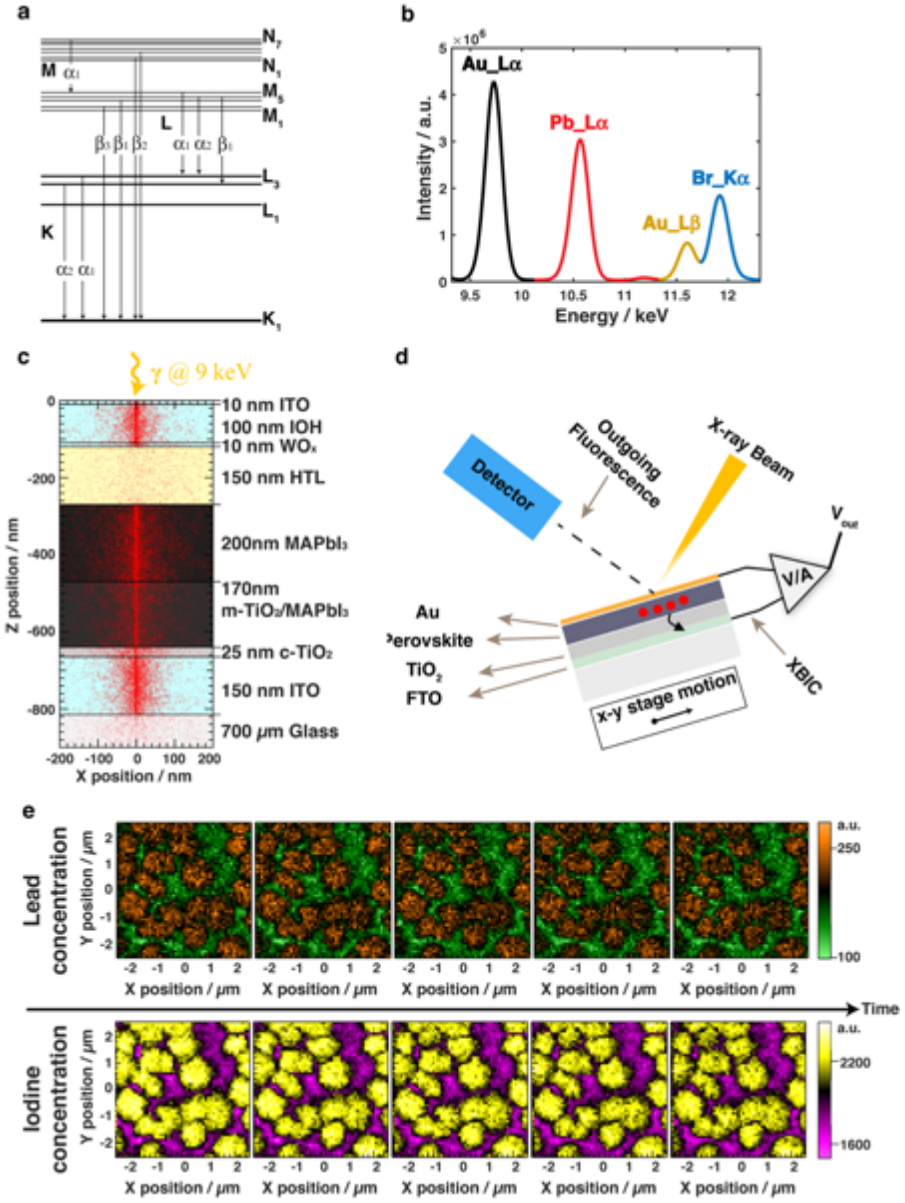


**Figure 4**. Experimental setup for nano-X-ray fluorescence (nano-XRF) mapping of nanoscale chemistry and X-ray beam induced current (XBIC) measurements of charge collection in perovskite solar cells. (a) nano-XRF operates by a mechanism where a high intensity X-ray beam removes a core-shell electron and the core-hole is filled by relaxation of one of an outer shell electron. (b) The elementally-specific fluorescence photons emitted are collected and produce an XRF spectrum of the elements irradiated locally under the X-ray nanoprobe. (c) A simulated end-of-trajectory profile of the interaction between a 9 keV X-ray photon and an $MAPbI_3$ perovskite film showing the narrow, nearly cylindrical excitation volume that provides a nanoscale probe of the film properties. (d) A bright synchrotron X-ray nanoprobe is used to investigate the elemental composition through the entire film stack in perovskite solar cells, penetrating through the backside metal contact. Excited carriers can thermalize to the band edges and be collected at the electrodes in complete perovskite devices – unaltered from standard architectures – using operando X-ray beam induced current. (e) 5x5 μm lead and iodine concentration maps (30 nm resolution) from repeated nano-XRF scans of a $MAPbI_3$ film are shown, indicating no observable changes upon extended X-ray irradiation. The relatively weak X-ray-matter interaction permits stable mapping of the perovskite chemistry. (c) Reproduced with permission.[123] Copyright 2016, IEEE.

### 3.4. X-ray Nanoprobes as A Window into Nanoscale Composition and Functionality

The working principle for nano-XRF is similar to EDX except an X-ray probe is used to generate characteristic X-rays – elementally-specific fluorescent photons (**Figure 4a**). When using a synchrotron radiation source, the energy of the incident X-ray beam is tuned to be above the binding energy of core shell electrons in elements of interest. The general working mechanism of XRF, an example of perovskite XRF spectra, and the schematic diagram of this *in-situ* experiment are present in **Figure 4b** and **4d.** Upon X-ray irradiation, the beam then excites core shell electrons, leaving behind a core hole that is rapidly filled by shallow-level electrons through X-ray fluorescence or Auger electron processes. In contrast to EDX, XRF is a photon-in and photon-out process, which results in a more sensitive and dose-efficient generation of elementally-specific X-ray photons. The brightness of 3rd generation synchrotron sources enables the X-ray beam to be focused down to probes as small as 11 nm in size[124] using diffractive optics while maintaining high flux density to achieve attogram sensitivity.[125,126]

The high sensitivity of nano-XRF has enabled detection and detailed study of trace constituents or impurities in a wide variety of materials, ranging from biological to impurities in organic[127] and inorganic solar cells.[128–131] Na is typically the lightest detectable element in practice using X-ray fluorescence. Heavier elements are much more easily detected, aided by the roughly $Z^4$ dependence of X-ray absorption on atomic number and the higher fluorescence yield relative to Auger decay at higher Z.[132] Unfortunately for hybrid perovskite studies, this Z-dependence means that the organic components are not detectable, though the composition and distribution of the inorganic A-site cations (*e.g.* $K^+$,$Cs^+$, $Rb^+$),[133,134] B-site metals, and the halides can be studied. In addition to typically reducing material damage relative to E-beam investigation, the reduced X-ray-matter interaction of XRF also has the advantage of probing

material that is buried under various layers in complex device architectures because of its long penetration depth (Figure 4b).

Benchtop and synchrotron-based X-ray diffraction measurements have also been used to probe the evolution of the structure of the material as a function of chemistry, hydration[99] and as a function of temperature and irradiation.[135] Diffraction provides valuable insights but offers only area- and thus chemically-averaged data because of the large spot sizes. X-ray photoemission spectroscopy (XPS) has also provided critical insights into chemical state and valence band edge alignments,[136,137] but the measurement is only sensitive to the first few nanometers near the sample surface and requires high vacuum conditions.[138]

Alternatives to probe film composition at the nanoscale include destructive approaches such as secondary ion mass spectroscopy (SIMS) and atom probe tomography (APT). SIMS is valuable for providing the elemental distribution profiles as a function of depth or in plane via mapping nano-SIMS[139] or TOF-SIMS[140] but it often involves sample fragmentation.[141] The APT technique is similar in principle to SIMS but is extremely powerful in that it can resolve single atoms in three spatial dimensions.[142] Unfortunately, the specimen preparation for APT is much more difficult and requires the careful use of focused ion beam (FIB) to prepare a submicron needle-like sample without affecting the specimen.[142,143] Recently, a laser assisted APT analysis provided supporting evidence of water accumulation in the hole transport layers (HTLs) within hybrid perovskite device after long term exposure, over 1000 hours, in ambient environment.[144] A recently published review by Hoye *et al* provides a summary of these techniques and best practices for applying them to perovskites.[145]

The non-destructive nature of X-ray based characterization means it has already seen wide application in hybrid perovskite materials, particularly using the bright and tunable sources available at synchrotrons. Cl was positively identified in processed perovskite thin films using bench top XRF and synchrotron-based X-ray absorption near edge structure (XANES), which provide area-averaged elemental and chemical information respectively.[146,147] In our

previous study,[148] spatially heterogeneous Cl incorporation was found in perovskite films, with Cl-rich regions forming near the perovskite crystallites boundaries by means of nano-XRF mapping with 30 nm resolution.[149] Critically, we demonstrated that the elemental distribution measured by nano-XRF was not affected by the probe itself upon repeated X-ray mapping.

Nano-XRF can be quantified using NIST-traceable XRF calibration standards that have known elemental loadings with 5-10% uncertainty in elemental concentrations depending on the element.[150] For greatest accuracy, these standards are measured immediately before or after the experimental sample using the same sample-detector geometry. The propagation of uncertainty from all possible errors during data quantification process thus has an optimistic lower bound error of 10%. The uncertainty in elemental concentration depends upon the dilution of the elements of interest and architecture of the sample under investigation, particularly upon the uniformity in thickness of the device layers. Quantification of trace elements in low-absorption matrices, such as transition metal impurities like iron and chromium in silicon solar cells, is straightforward.[151,152] Films where the major elements are of interest, like the halide perovskites, require attenuation corrections to accurately quantify results, with correction factors increasing in magnitude as film thickness increases.[153] The standards and any correction factors are applied for quantification after background subtraction and elemental peak-fitting of the XRF spectra, which is typically carried out using purpose built software.[154–158]

Fortunately, the strong optical absorption of halide perovskites means that their several hundred nanometer films require relatively smaller corrections than other solar absorbers such as CIGS. In general, the precision of a particular measurement can be significantly higher than the absolute accuracy. For the analysis of halide perovskite devices, we thus emphasize within-sample analysis and comparison of samples produced using identical processes. The quantification process for nano-XRF as applied for thin film solar cells was recently reported in detail in a visualized experiment to facilitate use by the broader community.[159]

Excited carriers generated by the X-ray irradiation can be collected as X-ray beam induced current,[160,161] the X-ray analog of EBIC and LBIC measurements. Upon X-ray irradiation, photo- and Auger-electrons radiate through the sample bulk. After a cascading loss of energy and thermalization, ultimately a single X-ray photon generates a much larger population of conduction band electrons and valence band holes.[149,162] The resulting number, $N$, of band-edge carriers is a function of the material, but has been empirically related to the energy of the incident X-ray photon, $E_x$, and the bandgap, $E_g$, according to the equation $N \approx E_x/3E_g$.[149,163] Thus for a typical characteristic hard X-ray energy of 10 keV and a bandgap on the order of 1 eV, the flux of the ionizing radiation is amplified by a factor of $10^3$ in generating photo-excited carriers. XBIC involves the collection of photocurrent induced by the X-ray beam's irradiation of the sample. In part, XBIC's utility stems from the ease of measurement of nano-or picoampere XBIC currents induced at high-resolution nanoprobes, though the device must be grounded appropriately to isolate the XBIC signal.[149] Because of the lower X-ray-matter interaction relative to electron beams, the incident X-ray has a larger penetration depth as compared laser or e-beam. A typical end-of-trajectory profile for X-ray irradiation in perovskites is shown in **Figure 4c**.[123] XBIC is the integrated current collected from the cylindrical excitation volume that extends through the entire film thickness.

### 3.5. *In-situ* Measurement of Elemental Distribution and Its effect on Charge Collection: Nano-XRF/XBIC

In applying nano-XRF/XBIC to hybrid perovskite studies, we typically probe our fully-operational solar cells through the thin Au back contact layer (Figure 4d). The bright synchrotron light source penetrates through the Au layer and reaches the perovskite absorber layer underneath it. This light-matter interaction generates not only the elemental specific X-ray photons but also excites charge carriers. The separated charge carriers are collected through the Au and FTO contacts and yield the electronic signal of the induced current. These *operando*

measurements enable us to relate the variation of nanoscale electronic performance with chemical compositional variations and identify directions within the compositional space for device improvement. To account for variations in carrier generation spatially in order to extract information regarding charge collection behavior, we normalized the XBIC using the local material's X-ray absorption coefficient and the bandgap as a function of its nanoscale chemical composition (a recent review of the XBIC technique provides further details[149]).

Perovskite film characterization is a challenge almost regardless of the experimental probe because of the material instability, and the characterization must be conducted carefully with optimized parameters to ensure measurements are properly attributed to the active perovskite phase and to avoid or quantify any degradation effects. For example, a recent study by Hoye *et al.*[145] found that the characterization environment could impact perovskite stability under irradiation significantly. The diffraction intensity of the perovskite (002) peak remained relatively unchanged when XRD characterization was conducted in helium condition, but linearly decreased when characterization was performed in air. Nano-XRF is typically carried out in helium to minimize attenuation due to atmospheric argon or in vacuum to further protect the zone plate optics against oxidation under high X-ray dose. The characterization windows for synchrotron-based hard X-ray nano-XRF and XBIC were first compiled by Stuckelberger *et al.* as shown in **Figure 4e**. Five repetitions under the highest X-ray flux density available in the Western hemisphere at beamline 26-id-c at APS revealed *no changes in the X-ray elemental map* at the strongest beam focus (30 nm spot size) even for the delicate $MAPbI_3$ perovskite chemistry. Although the composition extracted from XRF has proven to be stable under the high flux X-ray beam, it is likely that atomic-scale defects are generated under X-ray irradiation. In part, defect generation is evidenced by the decay of a simultaneously collected XBIC signal, which provides an indication of the loss of electronic quality of the perovskite under X-ray irradiation since current collection is highly sensitive to defects. For $MAPbI_3$, the XBIC signal drops exponentially with a half-life of ~600 seconds, presumably due to point-defect generation

by the ionizing radiation. An exponential XBIC decay is observed, a dependence similar to that observed in EBIC measurements as reported by Klein-Kedem.[114] However, with a typical 1 second per point nano-XRF/XBIC scan time, many experiments fit easily within the characterization window.[123]

If the X-ray sensitivity of the perovskite film does become limiting, we adopt a two-step strategy to achieve successful nano-XRF/XBIC measurements. We first perform an "electronic" measurement map, followed by an "elemental" map. For the electronic map, we combine high-throughput fly-scanning mapping that reduces scanning time to a typical 20-50 *ms* per point dwell time[164] and insert beam attenuation filters to reduce X-ray dose. This strategy takes advantage of the ~$10^3$ multiplication factor of band edge electrons generated per single hard X-ray photon and the relative ease of low-noise amplification of pA current measurements. However, the significant reduction in dose reduces our XRF elemental sensitivity. As necessary to improve our XRF signal-to-noise to strengthen any correlation between the nanoscale chemistry and the charge collection, following XBIC electronic measurement, we re-map the area for X-ray fluorescence at full flux and typically with a larger per point dwell time to achieve a high signal-to-noise ratio of the elemental distributions. These largely generalizable characterization strategies have enabled us to investigate the relationship between nanoscale chemistry and charge collection in the hybrid perovskites.[123]

## 4. The Impact of Chemical Heterogeneity within Hybrid Perovskites

Here we review our latest understanding of the heterogeneous elemental distribution within hybrid perovskite thin films and the impact of stoichiometric variations on device performance through the lens of X-ray nanoprobe characterization. A heterogeneous compositional distribution arises due to the structural flexibility of the perovskite materials. Somewhat surprisingly, even films with the simplest of hybrid chemistries, $MAPbI_3$ and $MAPbBr_3$, exhibit an inhomogeneous halide distribution. To illustrate the impact of these

variations in elemental distribution on device performance, we first summarize the impact of halide distribution on nanoscale charge collection and PL for single trihalide perovskites. We then incorporate new results from mixed halide perovskite studies using *in-situ* μ-XRF/XBIC techniques. We examine studies of heterogenous halide distribution and charge collection within complex mixed halide hybrid lead perovskite systems with $MAPbI_{3-x}Cl_x$ and $FAPbI_{3-x}Br_x$. Finally, we will provide first insights into the contribution of mixed A-site inorganic cations.

### 4.1. Insights from the Simplest Hybrids: Non-stoichiometry in $MAPbI_3$ and $MAPbBr_3$ Thin Film Devices Negatively Affects Charge Collection

Hybrid perovskite devices are surprisingly susceptible to halide non-stoichiometry. Recent studies tuning the excess amount of $PbI_2$ precursor in solution-processed perovskite thin film synthesis indicate there are clear trade-offs to having both a shortage of $PbI_2$ (loss in Jsc) and an excess (loss in $V_{oc}$), with the optimal performance coming from devices with a small 5% excess of $PbI_2$.[165] Spatially-resolved μ-XRF maps of heavy element constituents of lead (Pb) and iodine (I) in $MAPbI_3$ devices and the corresponding XBIC current provide some basis for microscopic understanding of the impact of lead-halide non-stoichiometry and are presented in **Figure 5**.[123] This $MAPbI_3$ absorber is deposited in a standard architecture atop $TiO_2$ scaffold with subsequent deposition of a Spiro-MeOTAD HTL. The nano-XRF study used a 30 nm X-ray probe available under vacuum at APS beamline 26-id-c. Using a watershed analysis, the film is separated into iodine rich and iodine poor regions. The Pb:I ratio map illustrates the inhomogeneous elemental distribution clearly, in which a Pb-rich hot spot with Pb:I ratio of 0.39 ± 0.03 (mean ± standard deviation) is detected while the rest of the film has a stoichiometric ratio of 0.29 ± 0.03, in good agreement within experimental uncertainty of the expected $MAPbI_3$ ratio of 0.33. Although the average Pb:I ratio of the Pb-rich area does not yield the exact expected ratio of 0.5 for a secondary $PbI_2$ phase, it is reasonable to expect there

may be some mix of $MAPbI_3$ and $PbI_2$ along the X-ray beam path through the sample thickness. At a minimum, the hotspot indicates second phase formation in the film and the Pb-rich local stoichiometry suggests it is $PbI_2$, which is known to be one of the decomposed products from $MAPbI_3$ perovskites.[166,167] The effect of the halide stoichiometry and local electronic performance is revealed when comparing the XRF chemical ratio map to the XBIC electronic map directly. The iodine poor regions correspond with low XBIC regions, indicating lower current collection, in good agreement with the lower short-circuit current found in devices using $PbI_2$-deficient synthesis.[165]

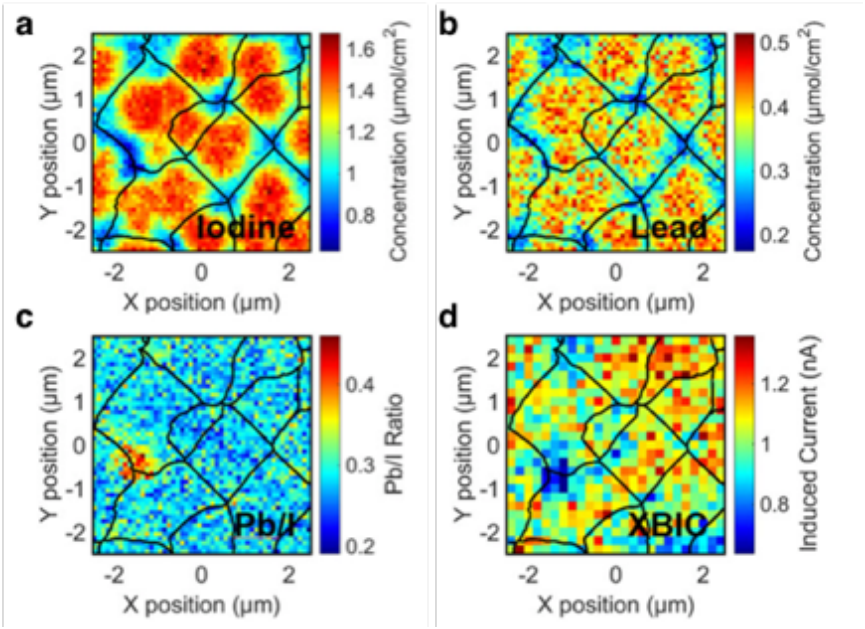


**Figure 5.** Nano-XRF and XBIC investigation of $MAPbI_3$. (a,b) Spatially resolved nano-XRF map of heavy element constituents, I and Pb, within a $MAPbI_3$ device. The scanned area is 5x5 µm with a 30 nm beam spot size. Watershed analysis shows the intragranular areas of high concentration, and the grain boundaries are highlighted by black lines. (c) A Pb:I molar ratio map of the same data reveals the heterogeneous stoichiometry across the film. The nominal stoichiometry should be Pb:I = 0.33, but varies significantly within the grains and between grains. An area of likely $PbI_2$ formation appears as a hotspot. (d) The X-ray beam induced current (XBIC) map shows that the lead-rich regions appear to collect charge poorly. Reproduced with permission.[149] Copyright 2017, Cambridge University Press.

Moving to the more robust bromide perovskite enabled *operando* µ-XRF/XBIC characterization technique to be extended to larger area mappings to obtain more statistical information regarding halide non-stoichiometry and its electronic influence. A $MAPbBr_3$ perovskite device was measured using X-ray beam with 250 nm spot size at APS 2-ID-D under

a helium ambient. This $MAPbBr_3$ cell does not contain an HTL layer, which is slightly different from the conventional architecture, but results in high-voltage bromide cells.[168] The local bromide-lead stoichiometry and the corresponding normalized XBIC current maps are presented in **Figure 6a** and **6b**, respectively. From the spatially resolved Br:Pb map, Br is found to be heterogeneously distributed, where it has a wide range of point-by-point molar ratio from 2.25 to 2.85 with an average measured stoichiometry of 2.6 and standard deviation of 0.09. It is a challenge to established that this film is indeed sub-stoichiometry on average given the XRF quantification uncertainty to be >10%. This number is in line with studies that have characterized the final thin film composition of perovskite films where an uncertainty of 7 to 10% of the average ratio has been reported.[138,169] However, a composition-spread investigation of mixed iodide-bromide perovskites also revealed systematically increasing sub-stoichiometry with increasing bromide content up to $MAPbI_2Br$ ((Br+I):Pb of 2.6 in $MAPbI_2Br$).[91] It is important to realize that, in addition to possible average sub-stoichiometry, the relative variation of Br:Pb stoichiometry within the same film revealed by nano-XRF is considerable.

A similar heterogeneity is observed in the current collection map in Figure 6b. We display a normalized XBIC map that accounts for differences in local absorption due to thickness variations.[149] To assess the correlation between halide distribution and local carrier collection, the normalized XBIC map is divided into 10 x 10 boxes, and the average value within each box of the normalized XBIC signal is plotted against the corresponding average Br:Pb ratio in **Figure** 6c. Figure 6c displays a positive correlation ($r^2$=0.41) between charge collection and the Br:Pb ratio. Carrier diffusion into neighboring pixels likely weakens the observed correlation, but the positive correlation is still recognizable from either visual inspection of the Br:Pb ratio map and the normalized XBIC map, or the scatter plot. The poor current collection can be attributed to areas of microscopic non-stoichiometry and, in some cases, the presence of small nuclei of $PbBr_2$ from perovskites decomposition seen as the darkest spots in Figure 6a. Clearly, more stoichiometric areas within both $MAPbI_3$ and $MAPbBr_3$ films

exhibit better current collection, and the current collection is quite sensitive to nanoscale chemistry. The question arises whether the impact of non-stoichiometry is due only to the presence of grain boundaries as extrinsic structural defects or whether non-stoichiometry has intrinsic impacts in the hybrid perovskites.

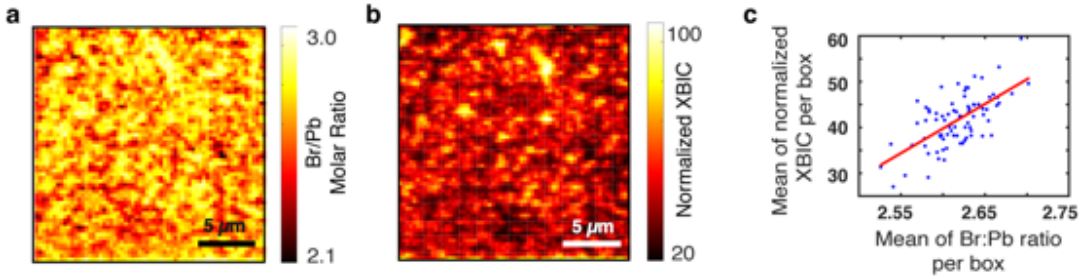


**Figure 6.** The influence of non-stoichiometry in a $MAPbBr_3$ solar cell. (a) A Br:Pb molar ratio map measured via nanoprobe XRF reveals a heterogeneous Br distribution within an $MAPbBr_3$ thin film solar cell. Bright regions are stoichiometric, while darker regions are sub-stoichiometric. (b) A normalized XBIC map for the mapped area is shown, where the collected X-ray beam induced current (XBIC) is normalized to the thickness-dependent local absorption. Current collection varies highly across the film. (d) The correlation between nanoscale XBIC and Br:Pb ratio is shown, where the Br:Pb ratio map and the normalized XBIC maps are divided into 10 x 10 boxes and the average value within the box is plotted. A positive trend exists between more stoichiometric MAPbBr3 and current collection probability.

### 4.1.1. A Critical Insight: Halide Migration and Resulting Non-Stoichiometry Results in Increased Carrier Recombination in *Single-Crystal* Perovskites

Using micron-scale single crystal model materials, we recently have shown that halide migration directly affects carrier recombination in $MAPbBr_3$.[170] Ion migration is proposed as an important limiting mechanism in hybrid organic inorganic perovskite (HOIP) devices because of hysteresis[21,171,172] and photo-induced instability.[23,173] Despite concerns regarding ion migration, many open questions remain as to its fundamental mechanism[174] and how stoichiometric changes[165,175] upon migration relate to device performance. A number of indirect approaches, particularly using electronic hysteresis scanning coupled with kinetics modeling, have suggested halide migration is the likely mechanism of device hysteresis.[176,177]

To take a step further, we used $MAPbBr_3$ single crystal to study ionic migration, which has been recognized to be one of the possible mechanisms that cause secondary phase formations in the perovskite system under applied electric field.[178,179]

Using nano-XRF at APS 2-ID-D with 200 nm resolution, we mapped changes in the elemental distribution within microscale single crystals of $MAPbBr_3$, using the elementally-specific nature of X-ray fluorescence to identify changes in nanoscale elemental composition.[170] The $MAPbBr_3$ microcrystals (μ-Xtal) were synthesized using a facile polydimethylsiloxane stamping method that creates thin (<1 μm) crystals that are single crystals, as revealed by sensitive electron backscatter diffraction.[180] Using symmetric contacts in a patterned back contact geometry as shown in **Figure 7a**, a thin $MAPbBr_3$ single crystal bridged lateral Pt-Pt electrodes, where the left-hand electrode was kept grounded. **Figure 7b** illustrates the direct observation of the lateral halide migration under bias from the μ-XRF mappings. Four μ-XRF images are arranged in chronological order from left to right that followed the bias sequence as listed below the Br:Pb elemental maps. The initial Br distribution is collected without applying any bias, yielding a homogeneous average Br:Pb molar ratio equal to ~3, as expected for a single crystal perovskite. After applying -2V bias, where the electric field pointed from left to right, bromide migration from right to left results in Br depletion above the right-hand electrode. Similar bromide depletion is observed above the left-hand electrode upon flipping the direction of the applied electric field. A noticeable amount of bromide is also recovered on the right-hand side. Lastly, the applied bias is switched to the first bias condition, -2V, and most of the Br depleted region is recovered on the left-hand electrode, while dark irreversible areas form on the right-hand Pt electrode. These irreversible areas indicate likely nanoscopic nuclei of $PbBr_2$ forming after repeating bias cycles and X-ray irradiation. Given the local formation of $PbBr_2$, we speculate that MABr leaves the sample in an electrochemical reaction resulting in overall Br loss, particularly during the first negative bias. Upon cycling of the bias condition, the overall trend within the sample is depletion of Br in the negatively-biased

region and recovery/accumulation of Br in the positively-biased region, consistent with bromide migration.[170]

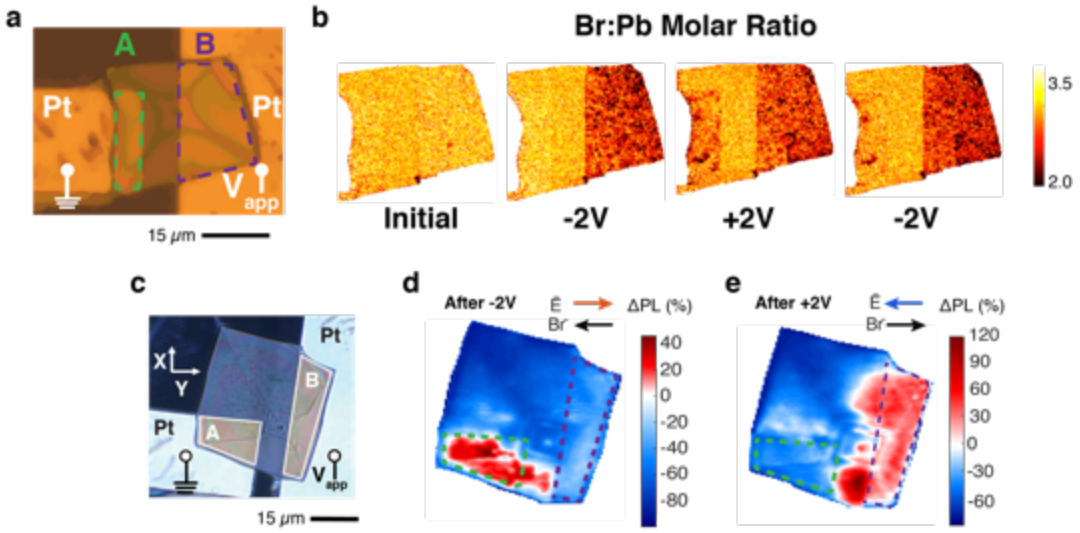


**Figure 7.** Direct observation of bromide migration in a single-crystal $MAPbBr_3$ thin film under applied bias. (a) Optical image of a microscale $MAPbBr_3$ single crystal deposited across back-contact Pt electrodes to enable in situ biasing. The left electrode is grounded for electrical biasing. (b) Nano-XRF measurements of the local Br:Pb ratio before bias and during a sequence of -2V, +2V, and -2V biasing. The shift in the Br content upon biasing reveals a quasi-reversible migration. (c) Optical image of a similar $MAPbBr_3$ used for μ-PL mapping. (d) μ-PL mapping after a return to 0V following a -2V bias shows that PL is enhanced in the region of Br enrichment and decreased in regions of Br depletion. (e) Subsequent biasing of the same crystal to +2V followed by relaxation reveals a shift of the PL hotspot to the opposite electrode, consistent with the direction of bromide migration. The correlation between the nano-XRF and PL data in single crystal perovskite materials suggests that halide migration and nanoscale halide non-stoichiometry play an important and intrinsic role in optoelectronic property within devices.[170]

Micro-photoluminescence (μ-PL) mapping of a fresh $MAPbBr_3$ crystal tied this bromide migration and the associated non-stoichiometry to carrier recombination activity. A similar bias sequence was applied to the crystal atop the same substrate as shown in **Figure 7c** and its spatially resolved μ-PL maps are shown in **Figure 7d** and **7e** respectively, showing the change in PL intensity after the same sequence of bias steps as during nano-XRF. PL intensity increases in halide-rich regions and decreases in halide-poor ones (Figure 7d).[170] Because PL is a measure of local excited carrier density, it correlates directly with local electronic quality. Br-rich regions thus exhibit lower recombination, while Br-depleted show higher recombination

activity. These results indicate a close relationship between halide vacancies and recombination activity. The direct link between halide migration and optoelectronic response clarifies that halide migration is a challenge that is *intrinsic* to the absorber and one that plays a determining role in the performance limits of perovskite devices. The average field applied (2 kV/cm, estimated from the ±2V applied bias across the 10 μm electrode gap) is at least one order of magnitude lower than the average field in operating hybrid perovskite thin film solar cells near their maximum power point. Mitigating halide migration is thus a necessary criterion for achieving stable perovskite optoelectronic performance. These correlative studies between μ-XRF and μ-PL suggests that halide migration is likely to occur under applied bias in operating cells and that nanoscale halide stoichiometry plays an important role in determining the optoelectronic properties within devices.[170] Developing strategies to mitigate ion migration and reduce defect density within perovskite thin films is necessary.

### 4.2. Mixing Cl and Br into Iodine-Rich Perovskites: Cl-Rich Regions are Benign and Br-Rich Regions are Efficient Current Collectors

Synthesis of mixed halide perovskite films has enabled improved solar cell efficiency, but open questions remain as to how the nanoscale chemistry determines performance in these films. Here, we analyze additions of Cl in $MAPbI_3$ and Br in $FAPbI_3$ thin films. It is now well-established that synthesis with Cl-containing precursors boosts the performance of $MAPbI_3$ devices.[116] The presence of Cl facilitates grain growth during perovskite crystallization due to the formation of small $PbCl_2$ nanocrystals that serve as nucleation centers, resulting in larger grain sizes.[25,181] The detection of remnant of Cl in the final film has been a challenge to further investigating the role of Cl. Benchtop X-ray fluorescence was used by Pool *et al*. to establish that Cl remained in the final film. X-ray absorption near edge spectroscopy confirmed that the remaining Cl adopts a chemical state distinct from either MACl or $PbCl_2$, suggesting it is chemically incorporated in some fashion into the film.[147] The distribution of Cl has also been

studied as a function of depth in the film by using X-ray photoelectron spectroscopy (HAXPES) and fluorescence yield X-ray absorption spectroscopy (FY-XAS).[182] The FY-XAS study found an inhomogeneous Cl distribution across the thin film thickness in $MAPbI_{3-x}Cl_x$, where no Cl was detected near sample surface but an upper limit estimate of Cl incorporation was established to be $0.07 < x < 0.4$ along the depth of 10 to 26 nm.

Using synchrotron based nano-XRF we identified a spatially heterogeneous incorporation of Cl in the plane of the perovskite film, finding a preferential accumulation of Cl at the boundaries of perovskite grains.[148] **Figure 8a** shows nano-XRF maps of two perovskite films: a film fabricated with two parts to one MACl:MAI in a two-step method (2:1, *2s*) and a film fabricated with equal parts MACl and MAI in a one-step synthesis (1:1, *1s*). Three elemental maps, Pb, I, and Cl, are shown normalized to the film's maximum to compare the relative distribution between samples. The map of Cl:I mass ratio indicates the sensitive Cl detection and shows that the final Cl concentrations in films are related to the amount of Cl-containing precursor introduced during the film synthesis. Furthermore, close inspection of the Cl:I mass ratio maps reveals that Cl distribution does not align with the major elements (Pb and I) in the film. This distinct distribution is shown more clearly for two randomly-selected crystallites in **Figure 8b**. The boundaries of the perovskite crystallites are generated by analysis of the I-rich regions evident in the I map. The Cl:I ratio maps for both crystallites suggest that Cl-rich regions are preferentially located adjacent to the perovskite crystallites (Column 3, Figure 6b).

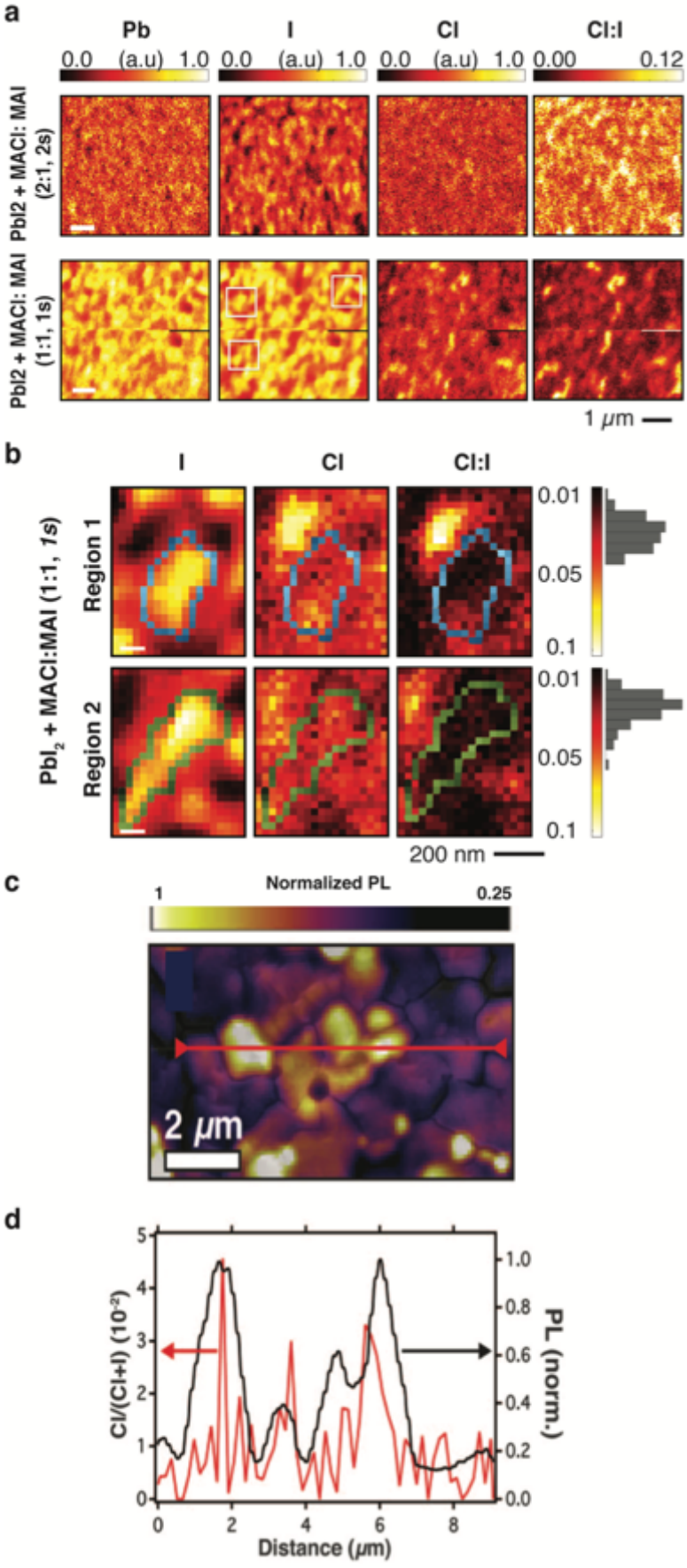


**Figure 8.** (a) Nano-XRF maps of Pb, I, Cl, and Cl:I ratio (left to right) in $MAPbI_{3-x}Cl_x$ films show a spatially heterogeneous incorporation of Cl in films made by two-step (top row) and

one-step (bottom row) methods. (b) High-resolution nano-XRF images of regions of randomly selected grains from the Cl-containing $PbI_2$ + MACl:MAI (1:1, 1s) sample. The highlighted boundary indicates the approximate outline of a single perovskite particle. Cl appears to accumulate predominantly at the boundaries or outside of iodide perovskite grains. (c) SEM image overlaid with spatially resolved μ-PL maps in $MAPbI_3$(Cl) film showing the negative impact of grain boundaries and the high degree of variation between grains. (d) EDS line scan of Cl/(Cl+I) weight ratio showing that Cl is associated with crystallites that have higher integrated PL intensity. (a) and (b) are reproduced with permission.[148] Copyright 2016, American Chemical Society. (c) and (d) are reproduced with permission.[1] Copyright 2015, Science.

Building from the detection of a varying Cl distribution within perovskite films, it is crucial to gain clearer insight into its nanoscale electronic impacts. deQuilettes *et al.* explored the role of Cl in $MAPbI_{3-x}Cl_x$ film by correlating SEM/EDX and μ-PL mapping.[1] Brighter PL regions are detected where Cl content is high as shown in **Figure 8c** and **8d.** However, the electronic role of Cl is still somewhat inconclusive. Other indirect effects due to presence of Cl, such as better crystal crystallinity, cannot be entirely neglected. For example, first-principles calculations indicate that Cl may play a role in passivating defect states at grain boundaries.[10] As an alternative to looking at PL of band-to-band recombination at open-circuit, we utilize nano-XRF/XBIC to look at a $MAPbI_{3-x}Cl_x$ device under charge-extracting short-circuit conditions as shown in **Figure 9**. A two-step deposition process was used to deposit perovskites on a mesoporous $TiO_2$ scaffold. The organic precursor solution had MAI:MACl = 2:1. The iodide map shows the individual grains and grain boundaries within the film, and the normalized Cl:I ratio map again indicates a highly heterogeneous distribution of Cl in the system **(Figure 9a** to **9c)**. The normalized XBIC appears to show enhanced charge collection in the thinnest part of the film near the grain boundaries **Figure 9d**. A plot of normalized XBIC vs. local Cl content is shown in **Figure 9e**. No correlation is found between the relative enrichment of Cl content and current collection. It seems that the Cl does not play a direct role in either enhancing carrier collection or preventing it. Instead, the data support arguments that the overall improvement on device performance and longer carrier lifetime upon addition of Cl

containing precursors are likely due to the indirect effect of improving crystal quality or enhancing surface/defect passivation.

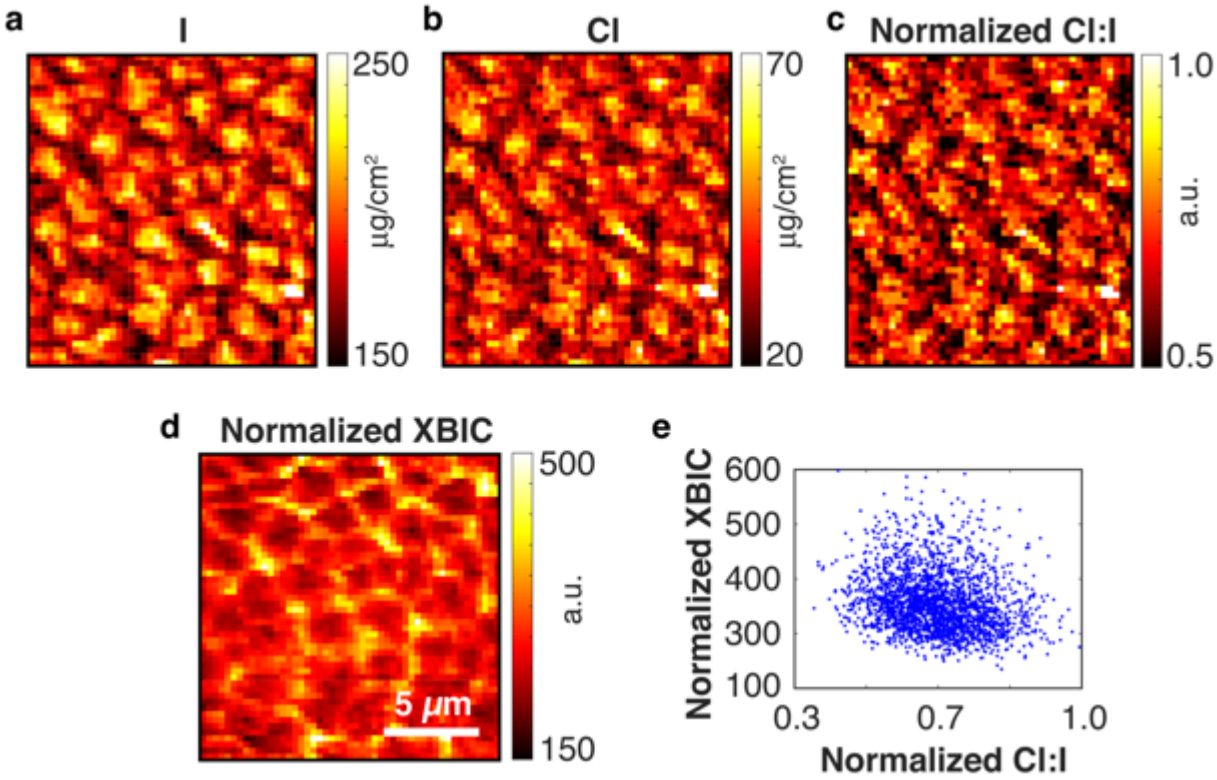


**Figure 9.** Nano-XRF/XBIC study of the optoelectronic role of Cl. (a-c) I, Cl, and normalized Cl:I nano-XRF maps illustrate the varying halide distribution within $MAPbI_{3-x}Cl_x$ films over many grains. (d) Normalized XBIC mapping of the same film shows strong variations in nanoscale charge collection. (d) Scatter plot of normalized XBIC and Cl:I mass ratio reveals little relationship local Cl incorporation and charge collection, indicating that the spatial variation in current collection is not a direct result of the Cl distribution.

### 4.2.1 Mixed Bromide-Iodides

The benign role of Cl raises questions regarding the role of Br in the widely-used mixed halides $MAPb(I_{1-x}Br_x)_3$ and $MA_{1-y}FA_yPb(I_{1-x}Br_x)_3$. As mentioned in Section 2, a small amount of Br incorporation benefits phase stability, the black phase of $FAPbI_3$ in particular.[20] The $FAPbI_{3-x}Br_x$ composition range has been studied in detail by Eperon *et al.* and Rehman *et al*, investigating the band gap tunability, phase stability and charge carrier dynamics at various levels of Br incorporation.[16,183] The band gap of the $FAPbI_{3-x}Br_x$ compositions can be tuned from 2.2 to 1.5 eV, with a shift from cubic to tetragonal phase as *x* varies from 0 to 1. An obstacle to homogenous chemical mixing is the crystal structure difference between the

tetragonal triiodide and cubic tribromide FA lead perovskites, and only a small fraction of Br can coexist and be incorporated to produce a stable film in the FA-based perovskites.[16] Perovskite films with higher Br:I ratio exhibit a reduction in crystallinity and even amorphization along with XRD peak shifting and boarding, particularly for the (110) tetragonal peak.[16,184] THz photoconductivity measurements at high Br incorporation (Br > 0.3) reveal that the regions of poor crystallinity that form due to the phase mismatch hinder charge-carrier transport with vanishing carrier mobility.[183]

Even in optimized 1:5 Br:I $MAPb(I_{0.2}Br_{0.8})_3$ perovskite films, abnormal optoelectronic behavior is observed including a reversible photo-induced trap formation in which the photoluminescence wavelength is red-shifted upon illumination[23,185] and hysteresis during JV measurements where the forward and reverse biased conditions produce JV curves particularly in the triiodide perovskites.[176,186] Multiple researchers have implicated ion migration[83,187] in combination with charge collecting at low-bandgap iodide-rich regions[188] to explain the local bandgap shifting under illumination. The intrinsic heterogeneity in bromide-iodide nanoscale chemistry in mixed-cation films has been evidenced indirectly by Kelvin Probe force microscopy with nanoscale potential fluctuations that are thought to fundamentally limit solar cell performance.[189]

Microscopic evidence of the nanoscale variations in chemistry and carrier collection underlying these important findings is provided by nano-XRF/XBIC investigation of $FAPbI_{3-x}Br_x$. **Figure 10** shows the nanoprobe XRF and XBIC maps for samples with different Br:I ratios ($x$=0.25 and 0.75). The Br incorporation is highly varied as seen in the Br:(Br+I) ratio maps in **Figure 10a** and **10b**. The average Br:(Br+I) ratio and its standard deviation for the nominally $FAPbI_{2.75}Br_{0.25}$ and $FAPbI_{2.25}Br_{0.75}$ films are 0.08 ± 0.01 and 0.25 ± 0.04, respectively, indicating good agreement between the average measured composition and the targeted composition. Though the characteristic grain sizes are smaller in the $x$=0.25 film than in the $x$=0.75 film, a similar degree of Br segregation is observed in both films, as quantified by a

coefficient of variation in Br:(Br+I) (standard deviation/average) of 0.17 for both $FAPbI_{2.75}Br_{0.25}$ and $FAPbI_{2.25}Br_{0.75}$. This high degree of heterogeneity is consistent with broadening of the (110) diffraction peak to 0.33 and 0.45° full-width half-maximum for $FAPbI_{2.75}Br_{0.25}$ and $FAPbI_{2.25}Br_{0.75}$ (not shown). The normalized XBIC electronic map accentuates the evident phase segregation within the films. Especially in the higher Br content $FAPbI_{2.25}Br_{0.75}$, large non-collecting regions are observed in **Figure 10c** and **10d.**

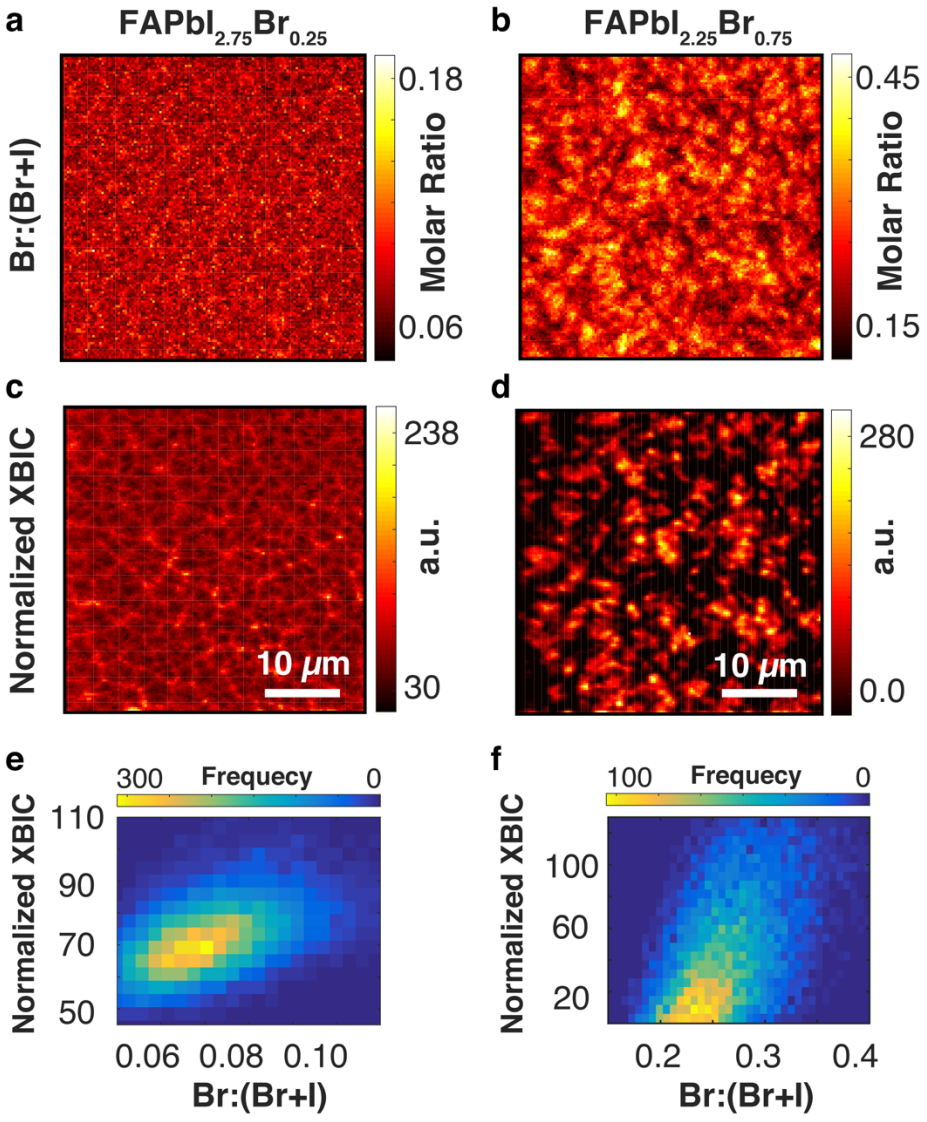


**Figure 10.** Halide distribution in $FAPbI_{3-x}Br_x$ and its impact on charge collection. (a,b) Nano-XRF maps showing the Br:Br+I ratio in films with x=0.25 and 0.75. Heterogeneity increases with *x* but is seen in both films. (c,d) Normalized *operando* XBIC maps reveal highly non-uniform charge collection, with some locals areas exhibiting far better current collection than others. Large fractions of the *x*=0.75 film show little photoresponse. (e,f) Two-dimensional

histograms of normalized XBIC vs Br:(Br+I) ratio for x = 0.25 and 0.75 show a positive correlation between local Br enrichment and current collection probability.

A two-dimensional histogram is used to illustrate the relation between Br incorporation and charge collection within each film as shown in **Figure 10e** and **10f**. In both cases, the regions within the film with higher Br content seems to yield better charge collection. This observation can be attributed to the band gap difference between $FAPbBr_3$ and $FAPbI_3$, in which the local regions of I-rich perovskite phase serve as sinks for generated carriers, with carriers generated in the Br-rich regions efficiently swept away and collected.[188] Although the Br-rich regions show improved charge collection, the tendency of mixed bromide iodide films to segregate on the nanoscale may limit the ability of these perovskites to reach their ultimate voltage limits due to bandgap-related Voc fluctuations.[189,190]

### 4.3. Effect of A-Site Cation for Controlling Film Morphology and Environmental stability

From an optoelectronic perspective, the incorporation of a different A-site cation in the 3D perovskite framework does not show as significant an impact on optical absorption nor photoluminescence peak shift as manipulating the lead halide bond (Figure 2c). However, the importance of A-site cations in controlling phase and environmental stability, especially in mixed halide perovskite, cannot be neglected. With a focus on recent investigation of A-site inorganic cations incorporation, double, triple and quadruple cations have been widely implemented to achieved long term stability as well as 20%+ photovoltaic efficiency.[9,70,72] In addition to the environmental stability mentioned in Section 2 for FA/Cs cation mixture, one important aspect of Cs incorporation is that it helps to suppress the photoinduced halide segregation in perovskite device as compared to the MA based mixed halide perovskites shown in **Figure 11a**. The control film of $MAPb(I_{0.6}Br_{0.4})_3$ displays a gradual photoluminescence shift from 1.80 to 1.68 eV under 1 hour light exposure with power density of ~ 3 mW/cm$^2$, while a constant PL peak at 1.72 eV is detected in a mixed A-site $FA_{0.83}Cs_{0.17}Pb(I_{0.6}Br_{0.4})_3$

composition.[185] Our early nano-XRF experiments investigating the nanoscale chemistry within such mixed-A-site films indicate that incorporation of Cs homogenizes the chemistry in the plane of the film (**Figure 11b**).

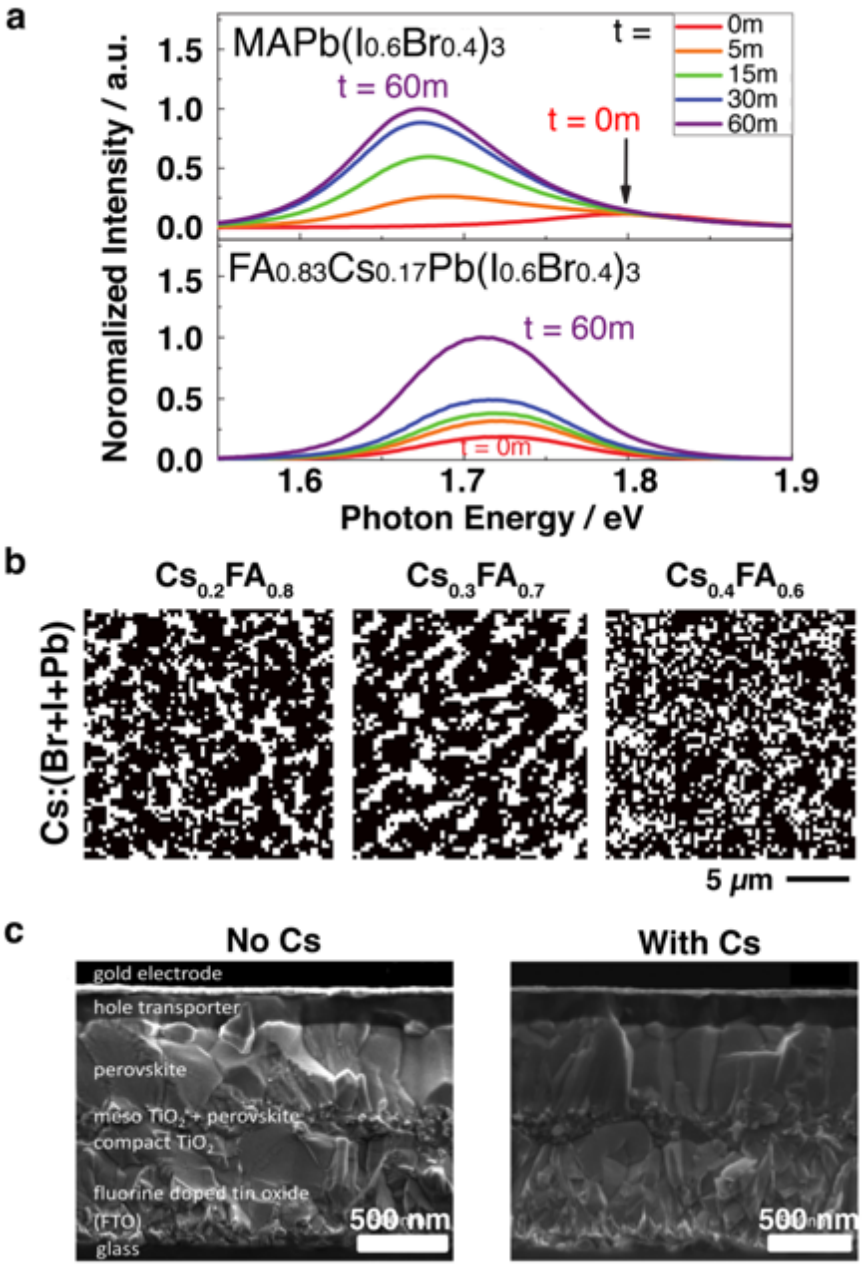


**Figure 11.** Early results on the role of mixed organic-inorganic A-site in determining nanoscale chemistry and performance. (a) Band-to-band photoluminescence measurements of $MAPb(I_{0.6}Br_{0.4})_3$ vs. $FA_{0.83}Cs_{0.17}Pb(I_{0.6}Br_{0.4})_3$ as a function of light exposure time show that Cs incorporation suppresses the change in emission wavelength linked to photo-induced halide segregation in mixed halide films. (b) Nano-XRF maps of $FA_{1-y}Cs_yPb(I_{0.8}Br_{0.2})_3$ films where y=0.2-0.4 that have been thresholded according to local Cs content into binary images. Increasing Cs loading gradually homogenizes the chemistry of perovskite thin films. (c) Cross-sectional SEM images of $MA_{0.17}FA_{0.83}Pb(I_{0.83}Br_{0.17})_3$ and $Cs_{0.05}(MA_{0.17}FA_{0.83})_{0.95}Pb(I_{0.83}Br_{0.17})_3$ show that Cs benefits the growth of grains that span the film thickness. (a) Reproduced with

permission.[185] Copyright 2016, Science. (c) Reproduced with permission.[17] Copyright 2016, Royal Society of Chemistry.

In addition to this homogenization, $Cs^+$ ions assist grain growth during perovskite film formation as shown in SEM images in **Figure 11c**. When no Cs containing precursor is introduced ($Cs_0M$, $(FAPbI_3)_{0.83}(MAPbBr_3)_{0.17}$), the perovskite grain growth is not directional nor monolithic, and grains have the tendency to stack on top of each other. On the other hand, when 5% of Cs containing precursor introduced, beneficial vertical grain growth is obtained. The uniform grain formation has been speculated to be a result of Cs-induced perovskite seeds that form at room temperature in precursor solution before spin coating.[17] Later in 2016, rubidium was introduced into the family of mixed A-site hybrid perovskites to form quadruple cation mixed halide perovskites.[9] The best performing Rb containing perovskite reaches PCE of 21.6%, and its environmental stability extends to 500 hours at 85 ˚C under full one sun illumination. Early indications via hard X-ray photoelectron spectroscopy are that Rb and Cs play complimentary roles in stabilizing perovskite thin films.[191] Further microscopic investigations are necessary to clarify the role of the inorganic cations in stabilizing the perovskite films and improving their performance.

## 5. Outlook and Conclusion

The emerging class of hybrid organic-inorganic perovskites offers disruptive potential for optoelectronic devices. The chemical flexibility of the perovskite structure has begun to be explored in the search for hybrid perovskites with tuned functional properties, with researchers implementing multiple substitutions to mix the composition of each of the constituent A, B, and X sites in materials of dimensionality varying from 0D quantum dots to nanowires and atomically-thin 2D layers to 3D films. Although truly impressive optoelectronic performance

has been achieved via this materials engineering, challenges remain to establish commercial viability for perovskite devices particularly regarding their performance variability and stability.

The chemical flexibility of perovskite benefits the optical absorption tunability in particular, but it often creates subsequent challenges in charge extraction in functional devices due to spatial heterogeneity in composition and phase segregation within or across devices. Accessing optoelectronic and chemical information at the nanoscale necessary to analyze these materials has proven difficult in part due to a significant effect of most probes on the very properties of the film under investigation. Researchers have applied widely varying methods to examine the unique and fascinating properties of the halide perovskites with at times heroic efforts necessary. We have highlighted only a small fraction of the many approaches and the insights gained, but provide a more detailed assessment of the relative merits of the most common probes: optical, e-beam, and X-ray. Regardless of characterization strategy, the community must establish rigorous metrics of probe-induced degradation in the perovskites, much as it has done regarding metrics for quantitative of perovskite solar cell device measurement.[192] Nanoscale characterization is necessary to build the detailed understanding of complex hybrid perovskite behavior required to overcome remaining stability and variability challenges to perovskite commercialization and extract the full potential out of the promising hybrid perovskite materials.

We focused here on recent nanoprobe X-ray investigations of elemental distribution via X-ray fluorescence combined with X-ray beam induced current collection measurements to identify the heterogeneous stoichiometry within perovskite films and the role of dopant/impurities on nanoscale charge collection within devices. We find that spatial variations in stoichiometry exist within even all-iodide and all-bromide thin film perovskite absorbers. *In situ* synchrotron-based X-ray nanoprobe measurements reveal direct evidence that halide poor regions result in lower charge collection. Nanoscale halide non-stoichiometry also manifesst itself during voltage biasing due to halide migration in methylammonium lead bromide

perovskite single crystals. The nanoscale non-stoichiometry that arises under bias negatively affects carrier lifetime, indicating that hybrid perovskites face *intrinsic materials challenges* beyond phase stability in ambient conditions. When mixing Br and I on the halide site, as is done in higher efficiency solar cells, we find that Br-rich areas exhibit enhanced local charge collection. On the other hand, local Cl incorporation does not seem to directly affect the local electronic properties. Finally, variations in the A-site stoichiometry within mixed Cs and formamidinium films show a larger impact on homogenizing the film than in determining nanoscale charge-carrier collection

Many open questions remain where nanoscale characterization holds promise for proving unique insight, such as the role of structural and phase defects in degradation, the electronic and chemical interactions at contact interfaces, as well as the microscopic electronic and chemical impact of recently investigated metal substitutions in halide perovskites. Small concentrations (<1%) of metal dopants in hybrid lead halide perovskites, $Al^{3+}$ and $Co^{2+}$ in particular, have exhibited positive benefits, such as reduction in non-radiative recombination and improvement of crystal growth that results in improved electronic quality or film morphology, though detrimental effects are observed at higher concentrations.[193–195] Thermal stability improvements are seen when using $Mn^{2+}$ as a B-site metal dopant in cesium lead halide perovskites.[196] Metal-substituted lead halide perovskites have also shown early promise for application in intermediate band photovoltaics.[197] Microscopic characterization pairing chemical and optoelectronic insights should advance understanding of the fundamental roles of these dopants and enable researchers to fully exploit the efficiency potential of perovskite optoelectronic devices.

The sensitivity of the functional properties of perovskites to ambient environments motivates further development of i*n situ* and *operando* characterization platforms that can provide direct evidence and a more precise and comprehensive understanding of the relationship between device behavior and nanoscale chemical or structural variations.

Researchers must consider perhaps not only how to mitigate these variations but also how future efforts might take advantage of this tendency in order to engineer novel device functionality or enhanced performance. Understanding how the nanoscale chemistry in complex hybrid perovskite thin films affects charge collection at the nanoscale scale is necessary to push the performance of perovskite optoelectronic devices toward their theoretical limits.

**Acknowledgements**
The authors thank Martin V. Holt and Peter Fuesz for helpful discussions in operation at APS 26-ID-C. D.P.F. acknowledges the support of a Hellman Fellowship. Y.L. and D.P.F. acknowledge the support of a California Energy Commission Advance Breakthrough award (EPC-16-050). MS and MB acknowledge support from the National Science Foundation (NSF) and the Department of Energy (DOE) under NSF CA No. EEC-433 1041895. This research used resources of the Advanced Photon Source, a U.S. Department of Energy (DOE) Office of Science User Facility operated for the DOE Office of Science by Argonne National Laboratory under Contract No. DE-AC02-06CH11357. Any opinions, findings and conclusions, or recommendation expressed in this material are those of the author(s) and do not necessarily reflect those of NSF or DOE.

Received: ((will be filled in by the editorial staff))
Revised: ((will be filled in by the editorial staff))
Published online: ((will be filled in by the editorial staff))

References

[1] D. W. deQuilettes, S. M. Vorpahl, S. D. Stranks, H. Nagaoka, G. E. Eperon, M. E. Ziffer, H. J. Snaith, D. S. Ginger, *Science* **2015**, *348*, 683.
[2] K. Wojciechowski, S. D. Stranks, A. Abate, G. Sadoughi, A. Sadhanala, N. Kopidakis, G. Rumbles, C. Z. Li, R. H. Friend, A. K. Y. Jen, H. J. Snaith, *ACS Nano* **2014**, *8*, 12701.
[3] Z.-K. Tan, R. S. Moghaddam, M. L. Lai, P. Docampo, R. Higler, F. Deschler, M. Price, A. Sadhanala, L. M. Pazos, D. Credgington, F. Hanusch, T. Bein, H. J. Snaith, R. H. Friend, *Nat. Nanotechnol.* **2014**, *9*, 1.
[4] H. Zhu, Y. Fu, F. Meng, X. Wu, Z. Gong, Q. Ding, M. V Gustafsson, M. T. Trinh, S. Jin, X.-Y. Zhu, *Nat. Mater.* **2015**, *14*, 636.
[5] H. Wei, Y. Fang, P. Mulligan, W. Chuirazzi, H.-H. Fang, C. Wang, B. R. Ecker, Y. Gao, M. A. Loi, L. Cao, J. Huang, *Nat. Photonics* **2016**, *10*, 333.
[6] Q. Dong, Y. Fang, Y. Shao, P. Mulligan, J. Qiu, L. Cao, J. Huang, *Science* **2015**, *347*, 967.
[7] D. Shi, V. Adinolfi, R. Comin, M. Yuan, E. Alarousu, A. Buin, Y. Chen, S. Hoogland, A. Rothenberger, K. Katsiev, Y. Losovyj, X. Zhang, P. A. Dowben, O. F. Mohammed, E. H. Sargent, O. M. Bakr, *Science* **2015**, *347*, 519.
[8] B. Yang, O. Dyck, J. Poplawsky, J. Keum, A. Puretzky, S. Das, I. Ivanov, C. Rouleau, G. Duscher, D. Geohegan, K. Xiao, *J. Am. Chem. Soc.* **2015**, *137*, 9210.
[9] M. Saliba, T. Matsui, K. Domanski, J.-Y. Seo, A. Ummadisingu, S. M. Zakeeruddin,

J.-P. Correa-Baena, W. R. Tress, A. Abate, A. Hagfeldt, M. Gratzel, *Science* **2016**, *354*, 206.
[10] W.-J. Yin, T. Shi, Y. Yan, *Adv. Mater.* **2014**, *26*, 4653.
[11] W.-J. Yin, T. Shi, Y. Yan, *Appl. Phys. Lett.* **2014**, *104*, 63903.
[12] R. E. Brandt, V. Stevanović, D. S. Ginley, T. Buonassisi, *MRS Commun.* **2015**, *5*, 265.
[13] A. Kojima, K. Teshima, Y. Shirai, T. Miyasaka, *J. Am. Chem. Soc.* **2009**, *131*, 6050.
[14] H.-S. Kim, C.-R. Lee, J.-H. Im, K.-B. Lee, T. Moehl, A. Marchioro, S.-J. Moon, R. Humphry-Baker, J.-H. Yum, J. E. Moser, M. Grätzel, N.-G. Park, *Sci. Rep.* **2012**, *2*, 591.
[15] J. H. Noh, S. H. Im, J. H. Heo, T. N. Mandal, S. Il Seok, *Nano Lett.* **2013**, *13*, 1764.
[16] G. E. Eperon, S. D. Stranks, C. Menelaou, M. B. Johnston, L. M. Herz, H. J. Snaith, *Energy Environ. Sci.* **2014**, *7*, 982.
[17] M. Saliba, T. Matsui, J.-Y. Seo, K. Domanski, J.-P. Correa-Baena, M. K. Nazeeruddin, S. M. Zakeeruddin, W. Tress, A. Abate, A. Hagfeldt, M. Grätzel, *Energy Environ. Sci.* **2016**, *9*, 1989.
[18] National Renewable Energy Laboratory (NREL), Best Research-Cell Efficiencies **2017**.
[19] W. S. Yang, J. H. Noh, N. J. Jeon, Y. C. Kim, S. Ryu, J. Seo, S. I. Seok, *Science* **2015**, *348*, 1234.
[20] W. S. Yang, B.-W. Park, E. H. Jung, N. J. Jeon, Y. C. Kim, D. U. Lee, S. S. Shin, J. Seo, E. K. Kim, J. H. Noh, S. Il Seok, *Science* **2017**, *356*, 1376.
[21] H. J. Snaith, A. Abate, J. M. Ball, G. E. Eperon, T. Leijtens, N. K. Noel, S. D. Stranks, J. T. W. Wang, K. Wojciechowski, W. Zhang, *J. Phys. Chem. Lett.* **2014**, *5*, 1511.
[22] A. Dualeh, P. Gao, S. Il Seok, M. K. Nazeeruddin, M. Grätzel, *Chem. Mater.* **2014**, *26*, 6160.
[23] E. T. Hoke, D. J. Slotcavage, E. R. Dohner, A. R. Bowring, H. I. Karunadasa, M. D. McGehee, *Chem. Sci.* **2015**, *6*, 613.
[24] J. Yang, B. D. Siempelkamp, D. Liu, T. L. Kelly, *ACS Nano* **2015**, *9*, 1955.
[25] S. D. Stranks, H. J. Snaith, *Nat. Nanotechnol.* **2015**, *10*, 391.
[26] J. Berry, T. Buonassisi, D. A. Egger, G. Hodes, L. Kronik, Y. L. Loo, I. Lubomirsky, S. R. Marder, Y. Mastai, J. S. Miller, D. B. Mitzi, Y. Paz, A. M. Rappe, I. Riess, B. Rybtchinski, O. Stafsudd, V. Stevanovic, M. F. Toney, D. Zitoun, A. Kahn, D. Ginley, D. Cahen, *Adv. Mater.* **2015**, *27*, 5102.
[27] M. a. Green, A. Ho-Baillie, H. J. Snaith, *Nat. Photonics* **2014**, *8*, 506.
[28] A. H. Slavney, T. Hu, A. M. Lindenberg, H. I. Karunadasa, *J. Am. Chem. Soc.* **2016**, *138*, 2138.
[29] B. Saparov, D. B. Mitzi, *Chem. Rev.* **2016**, *116*, 4558.
[30] Y. B. Nian, J. Strozier, N. J. Wu, X. Chen, A. Ignatiev, *Phys. Rev. Lett.* **2007**, *98*, 3.
[31] M. Cherry, M. S. Islam, C. R. A. Catlow, Oxygen Ion Migration in Perovskite-Type Oxides. *J. Solid State Chem.* **1995**, *118*, 125–132.
[32] H. Zhou, Q. Chen, G. Li, S. Luo, T. Song, H.-S. Duan, Z. Hong, J. You, Y. Liu, Y. Yang, *Science* **2013**, *345*, 542.
[33] A. Barrows, A. Pearson, C. Kwak, A. Dunbar, A. Buckley, D. Lidzey, *Energy Environ. Sci.* **2014**, *7*, 2944.
[34] R. D. Shannon, *Acta Crystallogr. Sect. A* **1976**, *32*, 751.
[35] X. Li, J. Yang, Q. Jiang, W. Chu, D. Zhang, Z. Zhou, Y. Ren, J. Xin, *Electrochim. Acta* **2017**, *247*, 460.
[36] J. T. Jacobsson, J. P. Correa Baena, M. Pazoki, M. Saliba, K. Schenk, M. Grätzel, A. Hagfeldt, *Energy Environ. Sci.* **2016**, *9*, 1706.
[37] W. Yin, T. Shi, Y. Yan, W. Yin, T. Shi, Y. Yan, *Appl. Phys. Lett.* **2014**, *104*, 1.
[38] Y. Luo, F. A. Santos, T. W. Wagner, E. Tsoi, S. Zhang, *J. Phys. Chem. B* **2014**, *118*,

6038.
[39] J. Tilchin, D. N. Dirin, G. I. Maikov, A. Sashchiuk, M. V. Kovalenko, E. Lifshitz, *ACS Nano* **2016**, *10*, 6363.
[40] K. Tanaka, T. Kondo, *Sci. Technol. Adv. Mater.* **2003**, *4*, 599.
[41] C. R. Kagan, D. B. Mitzi, C. D. Dimitrakopoulos, *Science* **1999**, *286*, 945.
[42] D. B. Mitzi, C. A. Feild, Z. Schlesinger, R. B. Laibowitz, *J. Solid State Chem.* **1995**, *114*, 159.
[43] N. K. Noel, S. D. Stranks, A. Abate, C. Wehrenfennig, S. Guarnera, A.-A. Haghighirad, A. Sadhanala, G. E. Eperon, S. K. Pathak, M. B. Johnston, A. Petrozza, L. M. Herz, H. J. Snaith, *Energy Environ. Sci.* **2014**, *7*, 3061.
[44] C. C. Stoumpos, C. D. Malliakas, M. G. Kanatzidis, *Inorg. Chem.* **2013**, *52*, 9019.
[45] W. Liao, D. Zhao, Y. Yu, C. R. Grice, C. Wang, A. J. Cimaroli, P. Schulz, W. Meng, K. Zhu, R. G. Xiong, Y. Yan, *Adv. Mater.* **2016**, *28*, 9333.
[46] V. M. Goldschmidt, *Naturwissenschaften* **1926**, *14*, 477.
[47] G. Kieslich, S. Sun, A. K. Cheetham, *Chem. Sci.* **2014**, *5*, 4712.
[48] G. Kieslich, S. Sun, T. Cheetham, *Chem. Sci.* **2015**, *6*, 3430.
[49] L. Pauling, *J. Am. Chem. Soc.* **1929**, *51*, 1010.
[50] C. Li, X. Lu, W. Ding, L. Feng, Y. Gao, Z. Guo, *Acta Crystallogr. Sect. B Struct. Sci.* **2008**, *64*, 702.
[51] X. G. Zhao, D. Yang, Y. Sun, T. Li, L. Zhang, L. Yu, A. Zunger, *J. Am. Chem. Soc.* **2017**, *139*, 6718.
[52] N. Wang, L. Cheng, R. Ge, S. Zhang, Y. Miao, W. Zou, C. Yi, Y. Sun, Y. Cao, R. Yang, Y. Wei, Q. Guo, Y. Ke, M. Yu, Y. Jin, Y. Liu, Q. Ding, D. Di, L. Yang, G. Xing, H. Tian, C. Jin, F. Gao, R. H. Friend, J. Wang, W. Huang, *Nat. Photonics* **2016**, *10*, 699.
[53] M. Yuan, L. N. Quan, R. Comin, G. Walters, R. Sabatini, O. Voznyy, S. Hoogland, Y. Zhao, E. M. Beauregard, P. Kanjanaboos, Z. Lu, D. H. Kim, E. H. Sargent, *Nat. Nanotechnol.* **2016**, *11*, 872.
[54] H. Tsai, W. Nie, J.-C. Blancon, C. C. Stoumpos, C. M. M. Soe, J. Yoo, J. Crochet, S. Tretiak, J. Even, A. Sadhanala, G. Azzellino, R. Brenes, P. M. Ajayan, V. Bulovic´, S. D. Stranks, R. H. Friend, M. G. Kanatzidis, A. D. Mohite, *Adv. Mater.* **2017**, *1704217*, 1704217.
[55] C. C. Stoumpos, D. H. Cao, D. J. Clark, J. Young, J. M. Rondinelli, J. I. Jang, J. T. Hupp, M. G. Kanatzidis, *Chem. Mater.* **2016**, *28*, 2852.
[56] Y. Chen, Y. Sun, J. Peng, J. Tang, K. Zheng, Z. Liang, *Adv. Mater.* **2017**, *1703487*, 1.
[57] B. Cohen, M. Wierzbowska, L. Etgar, *Adv. Funct. Mater.* **2017**, *27*, 1604733.
[58] G. Grancini, C. Roldán-Carmona, I. Zimmermann, E. Mosconi, X. Lee, D. Martineau, S. Narbey, F. Oswald, F. De Angelis, M. Graetzel, M. K. Nazeeruddin, *Nat. Commun.* **2017**, *8*, 1.
[59] C. R. Kagan, *Science* **1999**, *286*, 945.
[60] J. H. Heo, D. H. Song, S. H. Im, *Adv. Mater.* **2014**, *26*, 8179.
[61] K. Osvald, R. E. Wasylishen, M. A. White, C. T. Stanley, M. J. M. Van Oort, *Can. J. Chem* **1990**, *68*, 412.
[62] D. Solis-Ibarra, I. C. Smith, H. I. Karunadasa, *Chem. Sci.* **2015**, *6*, 4054.
[63] C. Eames, J. M. Frost, P. R. F. Barnes, B. C. O'Regan, A. Walsh, M. S. Islam, *Nat. Commun.* **2015**, *6*, 7497.
[64] Y.-Y. Zhang, S. Chen, P. Xu, H. Xiang, X.-G. Gong, A. Walsh, S. Wei, *Nat. Commun.* **2015**, 11.
[65] N. J. Jeon, J. H. Noh, Y. C. Kim, W. S. Yang, S. Ryu, S. Il Seok, *Nat. Mater.* **2014**, *13*, 1.
[66] N. J. Jeon, J. H. Noh, W. S. Yang, Y. C. Kim, S. Ryu, J. Seo, S. Il Seok, *Nature* **2015**,

*517*, 476.
[67] K. A. Bush, C. D. Bailie, Y. Chen, A. R. Bowring, W. Wang, W. Ma, T. Leijtens, F. Moghadam, M. D. McGehee, *Adv. Mater.* **2016**, *28*, 3937.
[68] M. Kulbak, D. Cahen, G. Hodes, *J. Phys. Chem. Lett.* **2015**, *6*, 2052.
[69] M. Kulbak, S. Gupta, N. Kedem, I. Levine, T. Bendikov, G. Hodes, D. Cahen, *J. Phys. Chem. Lett.* **2016**, *7*, 167.
[70] H. Choi, J. Jeong, H. Kim, S. Kim, B. Walker, G. Kim, J. Young, *Nano Energy* **2014**, *7*, 80.
[71] J. Lee, D. Kim, H. Kim, S. Seo, S. M. Cho, N. Park, *Adv. Energy Mater.* **2015**, *5*, 1.
[72] Z. Li, M. Yang, J. Park, S. Wei, J. J. Berry, K. Zhu, *Chem. Mater.* **2016**, 284.
[73] C. Yi, J. Luo, S. Meloni, A. Boziki, N. Ashari-Astain, C. Gratzel, S. M. Zakeeruddin, U. Rothlisberger, M. Gratzel, *Energy Environ. Sci.* **2016**, *9*, 656.
[74] E. Edri, S. Kirmayer, S. Mukhopadhyay, K. Gartsman, G. Hodes, D. Cahen, *Nat. Commun.* **2014**, *5*, 1.
[75] B. El Cohen, M. Wierzbowska, L. Etgar, *Sustain. Energy Fuels* **2017**, *1*, 1935.
[76] F. Giordano, A. Abate, J. Pablo, C. Baena, M. Saliba, T. Matsui, S. H. Im, S. M. Zakeeruddin, M. K. Nazeeruddin, A. Hagfeldt, M. Graetzel, *Nat. Commun.* **2016**, *7*, 1.
[77] D. Bi, W. Tress, M. I. Dar, P. Gao, J. Luo, C. Renevier, K. Schenk, A. Abate, G. Fabrizio, J. C. Baena, J. Decoppet, S. M. Zakeeruddin, M. K. Nazeeruddin, M. Gratzel, A. Hagfeldt, *Sci. Adv.* **2016**, *2*, 1.
[78] M. Liu, M. B. Johnston, H. J. Snaith, *Nature* **2013**, *501*, 395.
[79] S. D. Stranks, G. E. Eperon, G. Grancini, C. Menelaou, M. J. P. Alcocer, T. Leijtens, L. M. Herz, A. Petrozza, H. J. Snaith, *Science* **2013**, *342*, 341.
[80] W. Ke, G. Fang, Q. Liu, L. Xiong, P. Qin, H. Tao, J. Wang, H. Lei, B. Li, J. Wan, G. Yang, Y. Yan, *J. Am. Chem. Soc.* **2015**, 6730.
[81] T. Matsui, W. Tress, M. Saliba, A. Abate, M. Gra, A. Hagfeldt, *Energy Environ. Sci.* **2016**, *9*, 3128.
[82] Q. Jiang, L. Zhang, H. Wang, X. Yang, J. Meng, H. Liu, Z. Yin, J. Wu, X. Zhang, J. You, *Nat. Energy* **2016**, *2*, 1.
[83] J. Pablo, C. Baena, L. Steier, W. Tress, M. Saliba, S. Neutzner, T. Matsui, F. Giordano, T. J. Jacobsson, A. Ram, S. Kandada, S. M. Zakeeruddin, A. Petrozza, A. Hagfeldt, *Energy Environ. Sci.* **2015**, *8*, 2928.
[84] W. Ke, D. Zhao, C. Xiao, C. Wang, A. J. Cimaroli, C. R. Grice, M. Yang, Z. Li, C. Jiang, M. Al-jassim, K. Zhu, M. G. Kanatzidis, G. Fang, Y. Yan, *J. Mater. Chem. A* **2016**, *4*, 14276.
[85] Y. Zhao, A. Nardes, K. Zhu, *Faraday Discuss.* **2014**, *176*, 301.
[86] T.-S. Su, T.-Y. Hsieh, C.-Y. Hong, T.-C. Wei, *Sci. Rep.* **2015**, *5*, 16098.
[87] A. Dualeh, N. Tétreault, T. Moehl, P. Gao, M. K. Nazeeruddin, M. Grätzel, *Adv. Funct. Mater.* **2014**, *24*, 3250.
[88] N. K. Noel, A. Abate, S. D. Stranks, E. S. Parrott, V. M. Burlakov, A. Goriely, H. J. Snaith, *ACS Nano* **2014**, *8*, 9815.
[89] Q. Chen, H. Zhou, T. Bin Song, S. Luo, Z. Hong, H. S. Duan, L. Dou, Y. Liu, Y. Yang, *Nano Lett.* **2014**, *14*, 4158.
[90] G. E. Eperon, D. Moerman, D. S. Ginger, *ACS Nano* **2016**, *10*, 10258.
[91] I. L. Braly, H. W. Hillhouse, *J. Phys. Chem. C* **2016**, *120*, 893.
[92] J. L. Garrett, E. M. Tennyson, M. Hu, J. Huang, J. N. Munday, M. S. Leite, *Nano Lett.* **2017**, *17*, 2554.
[93] N. Kedem, T. M. Brenner, M. Kulbak, N. Schaefer, S. Levcenko, I. Levine, D. Abou-Ras, G. Hodes, D. Cahen, *J. Phys. Chem. Lett.* **2015**, *6*, 2469.
[94] E. Article, E. Mosconi, F. De Angelis, H. I. Karunadasa, E. T. Hoke, A. Petrozza, *Chem. Sci.* **2015**, *6*, 7305.

[95] M. Anaya, M. E. Calvo, H. M, *J. Phys. Chem. Lett.* **2015**, *6*, 2200.
[96] H. Fang, S. Adjokatse, H. Wei, J. Yang, G. R. Blake, J. Huang, J. Even, M. A. Loi, *Sci. Adv.* **2016**, *2*, 1.
[97] R. Brenes, D. Guo, A. Osherov, N. K. Noel, C. Eames, E. M. Hutter, S. K. Pathak, F. Niroui, R. H. Friend, M. S. Islam, H. J. Snaith, V. Bulović, T. J. Savenije, S. D. Stranks, *Joule* **2017**, *1*, 155.
[98] C. Mu, T. Glaser, M. Plogmeyer, M. Sendner, S. Do, A. A. Bakulin, C. Brzuska, R. Scheer, M. S. Pshenichnikov, W. Kowalsky, A. Pucci, R. Lovrinc, *Chem. Mater.* **2015**, *27*, 7835.
[99] M. A. Leguy, Y. Hu, M. Campoy-quiles, M. I. Alonso, O. J. Weber, P. Azarhoosh, M. Van Schilfgaarde, M. T. Weller, T. Bein, J. Nelson, P. Docampo, P. R. F. Barnes, *Chem. Mater.* **2015**, *27*, 3397.
[100] G. N. Hall, M. E. Stuckelberger, T. Nietzold, J. Hartman, J.-S. Park, J. Werner, B. Niesen, M. L. Cummings, V. Rose, C. Ballif, M. K. Y. Chan, D. P. Fenning, M. I. Bertoni, *J. Phys. Chem. C* **2017**, *121*, 25659.
[101] C. R. McNeill, H. Frohne, J. L. Holdsworth, J. E. Furst, B. V. King, P. C. Dastoor, *Nano Lett.* **2004**, *4*, 219.
[102] H. Heinzelmann, D. W. Pohl, *Appl. Phys. A Solids Surfaces* **1994**, *59*, 89.
[103] Y. Kutes, Y. Zhou, J. L. Bosse, J. Steffes, N. P. Padture, B. D. Huey, *Nano Lett.* **2016**, *16*, 3434.
[104] R. Dong, Y. Fang, J. Chae, J. Dai, Z. Xiao, Q. Dong, Y. Yuan, A. Centrone, X. C. Zeng, J. Huang, *Adv. Mater.* **2015**, *27*, 1912.
[105] J. Hieulle, C. Stecker, R. Ohmann, L. K. Ono, Y. Qi, *Small Methods* **2017**, *1700295*, 1.
[106] O. Nichiporuk, A. Kaminski, M. Lemiti, A. Fave, S. Litvinenko, V. Skryshevsky, *Thin Solid Films* **2006**, *511–512*, 248.
[107] S. Mastroianni, F. D. Heinz, J.-H. Im, W. Veurman, M. Padilla, M. C. Schubert, U. Würfel, M. Grätzel, N.-G. Park, A. Hinsch, *Nanoscale* **2015**, *7*, 19653.
[108] Z. Song, J. Werner, N. Shrestha, F. Sahli, S. De Wolf, B. Niesen, S. C. Watthage, A. B. Phillips, C. Ballif, R. J. Ellingson, M. J. Heben, *J. Phys. Chem. Lett.* **2016**, *7*, 5114.
[109] H. Demers, N. Poirier-Demers, A. R. Couture, D. Joly, M. Guilmain, N. De Jonge, D. Drouin, *Scanning* **2011**, *33*, 135.
[110] K. Sakurai, H. Eba, K. Inoue, N. Yagi, *Anal. Chem.* **2002**, *74*, 4532.
[111] P. Hovington, D. Drouin, R. Gauvin, *Scanning* **1997**, *19*, 1.
[112] N. Chatterjee, In *Electron Microprobe Analysis*; MIT, Cambridge, 2012; pp. 12–20.
[113] A. R. Sakulich, V. C. Li, *33rd Int'l Conf Cem. Microsc. San Fr. CA USA* **2011**, *16*, 1.
[114] N. Klein-Kedem, D. Cahen, G. Hodes, *Acc. Chem. Res.* **2016**, *49*, 347.
[115] H. J. S. Michael M. Lee, Joel Teuscher, Tsutomu Miyasaka, Takurou N. Murakami, *Science* **2012**, *338*, 643.
[116] Q. Chen, H. Zhou, Y. Fang, A. Z. Stieg, T.-B. Song, H.-H. Wang, X. Xu, Y. Liu, S. Lu, J. You, P. Sun, J. McKay, M. S. Goorsky, Y. Yang, *Nat. Commun.* **2015**, *6*, 1.
[117] H. Yu, F. Wang, F. Xie, W. Li, J. Chen, N. Zhao, *Adv. Funct. Mater.* **2014**, *24*, 7102.
[118] J. Qing, H. T. Chandran, Y. H. Cheng, X. K. Liu, H. W. Li, S. W. Tsang, M. F. Lo, C. S. Lee, *ACS Appl. Mater. Interfaces* **2015**, *7*, 23110.
[119] S. T. Williams, F. Zuo, C. C. Chueh, C. Y. Liao, P. W. Liang, A. K. Y. Jen, *ACS Nano* **2014**, *8*, 10640.
[120] M. I. Dar, N. Arora, P. Gao, S. Ahmad, M. Gratzel, M. K. Nazeeruddin, *Nano Lett.* **2014**, *14*, 6991.
[121] O. Hentz, Z. Zhao, *Nano Lett.* **2016**, *16*, 1485.
[122] E. Edri, S. Kirmayer, A. Henning, S. Mukhopadhyay, K. Gartsman, Y. Rosenwaks, G. Hodes, D. Cahen, *Nano Lett.* **2014**, *14*, 1000.
[123] M. Stuckelberger, T. Nietzold, G. N. Hall, B. West, B. Niesen, C. Ballif, V. Rose, D. P.

Fenning, M. I. Bertoni, *IEEE J. Photovoltaics* **2017**, *7*, 590.
[124] X. Huang, H. Yan, E. Nazaretski, R. Conley, N. Bouet, J. Zhou, K. Lauer, L. Li, D. Eom, D. Legnini, R. Harder, I. K. Robinson, Y. S. Chu, *Sci. Rep.* **2013**, *3*, 1.
[125] D. Shu, J. Maser, B. Lai, S. Vogt, M. Holt, C. Preissner, A. Smolyanitskiy, B. Tieman, R. Winarski, G. B. Stephenson, *Proc. 8th Int. Conf. X-ray Microsc.* **2006**, *7*, 56.
[126] R. P. Winarski, M. V. Holt, V. Rose, P. Fuesz, D. Carbaugh, C. Benson, D. Shu, D. Kline, G. Brian Stephenson, I. McNulty, J. Maser, G. B. Stephenson, I. McNulty, J. Maser, *J. Synchrotron Radiat.* **2012**, *19*, 1056.
[127] M. P. Nikiforov, B. Lai, W. Chen, S. Chen, R. D. Schaller, J. Strzalka, J. Maser, S. B. Darling, *Energy Environ. Sci.* **2013**, *6*, 1513.
[128] T. Buonassisi, A. A. Istratov, M. A. Marcus, B. Lai, Z. Cai, S. M. Heald, E. R. Weber, *Nat. Mater.* **2005**, *4*, 676.
[129] M. I. Bertoni, D. P. Fenning, M. Rinio, V. Rose, M. Holt, J. Maser, T. Buonassisi, *Energy Environ. Sci.* **2011**, *4*, 4252.
[130] H. S. Laine, V. Vahanissi, A. E. Morishige, J. Hofstetter, A. Haarahiltunen, B. Lai, H. Savin, D. P. Fenning, *IEEE J. Photovoltaics* **2016**, *6*, 1094.
[131] A. E. Morishige, M. A. Jensen, J. Hofstetter, P. X. T. Yen, C. Wang, B. Lai, D. P. Fenning, T. Buonassisi, *Appl. Phys. Lett.* **2016**, *108*, 1.
[132] P. Willmott, *An Introduction to Synchrotron Radiation: Techniques and Applications*; John Wiley & Sons, Ltd, 2011.
[133] Z. Tang, T. Bessho, F. Awai, T. Kinoshita, M. M. Maitani, R. Jono, T. N. Murakami, H. Wang, T. Kubo, S. Uchida, H. Segawa, *Sci. Rep.* **2017**, *7*, 1.
[134] J. K. Nam, S. U. Chai, W. Cha, Y. J. Choi, W. Kim, M. S. Jung, J. Kwon, D. Kim, J. H. Park, *Nano Lett.* **2017**, *17*, 2028.
[135] L. T. Schelhas, J. A. Christians, J. J. Berry, M. F. Toney, C. J. Tassone, J. M. Luther, K. H. Stone, *ACS Energy Lett.* **2016**, *1*, 1007.
[136] P. Schulz, E. Edri, S. Kirmayer, G. Hodes, D. Cahen, A. Kahn, *Energy Environ. Sci.* **2014**, *7*, 1377.
[137] S. Siol, P. Schulz, M. Young, K. A. Borup, G. Teeter, A. Zakutayev, *Adv. Mater. Interfaces* **2016**, *3*, 1.
[138] C. Li, S. Tscheuschner, F. Paulus, P. E. Hopkinson, J. Kießling, A. Köhler, Y. Vaynzof, S. Huettner, *Adv. Mater.* **2016**, *28*, 2446.
[139] K. Sardashti, R. Haight, T. Gokmen, W. Wang, L. Y. Chang, D. B. Mitzi, A. C. Kummel, *Adv. Energy Mater.* **2015**, *5*, 1.
[140] S. P. Harvey, J. A. Aguiar, P. Hacke, H. Guthrey, S. Johnston, M. Al-Jassim, *IEEE J. Photovoltaics* **2016**, *6*, 1440.
[141] Z. Li, C. Xiao, Y. Yang, S. P. Harvey, D. H. Kim, J. A. Christians, M. Yang, P. Schulz, S. U. Nanayakkara, C.-S. Jiang, J. M. Luther, J. J. Berry, M. C. Beard, M. M. Al-Jassim, K. Zhu, *Energy Environ. Sci.* **2017**, *10*, 1234.
[142] A. Devaraj, D. E. Perea, J. Liu, L. M. Gordon, T. J. Prosa, P. Parikh, D. R. Diercks, S. Meher, R. P. Kolli, Y. S. Meng, S. Thevuthasan, *Int. Mater. Rev.* **2017**, *0*, 1.
[143] A. Cerezo, P. H. Clifton, M. J. Galtrey, C. J. Humphreys, T. F. Kelly, D. J. Larson, S. Lozano-Perez, E. A. Marquis, R. A. Oliver, G. Sha, K. Thompson, M. Zandbergen, R. L. Alvis, *Mater. Today* **2007**, *10*, 36.
[144] S. Wang, M. Sina, P. Parikh, T. Uekert, B. Shahbazian, A. Devaraj, Y. S. Meng, *Nano Lett.* **2016**, *16*, 5594.
[145] R. L. Z. Hoye, P. Schulz, L. T. Schelhas, A. M. Holder, K. H. Stone, J. D. Perkins, D. Vigil-Fowler, S. Siol, D. O. Scanlon, A. Zakutayev, A. Walsh, I. C. Smith, B. C. Melot, R. C. Kurchin, Y. Wang, J. Shi, F. C. Marques, J. J. Berry, W. Tumas, S. Lany, V. Stevanović, M. F. Toney, T. Buonassisi, *Chem. Mater.* **2017**, *29*, 1964.
[146] E. L. Unger, A. R. Bowring, C. J. Tassone, V. L. Pool, A. Gold-parker, R.

Cheacharoen, K. H. Stone, E. T. Hoke, M. F. Toney, M. D. Mcgehee, *Chem. Mater.* **2014**, *26*, 7158.
[147] V. L. Pool, A. Gold-Parker, M. D. McGehee, M. F. Toney, *Chem. Mater.* **2015**, *27*, 7240.
[148] Y. Luo, S. Gamliel, S. Nijem, S. Aharon, M. Holt, B. Stripe, V. Rose, M. I. Bertoni, L. Etgar, D. P. Fenning, *Chem. Mater.* **2016**, *28*, 6536.
[149] M. Stuckelberger, B. West, T. Nietzold, B. Lai, J. M. Maser, V. Rose, M. I. Bertoni, *J. Mater. Res.* **2017**, *32*, 1825.
[150] AXO DRESDEN Gmbh, *AXO XRF Standard.pdf*; 2014.
[151] D. P. Fenning, J. Hofstetter, M. I. Bertoni, G. Coletti, B. Lai, C. Cañizo, T. Buonassisi, *J. Appl. Phys.* **2013**, *113*, 44521.
[152] M. A. Jensen, J. Hofstetter, A. E. Morishige, G. Coletti, B. Lai, D. P. Fenning, T. Buonassisi, *Appl. Phys. Lett.* **2015**, *106*, 0.
[153] B. M. West, M. Stuckelberger, A. Jeffries, S. Gangam, B. Lai, B. Stripe, J. Maser, V. Rose, S. Vogt, M. I. Bertoni, *J. Synchrotron Radiat.* **2017**, *24*, 288.
[154] C. G. Ryan, B. E. Etschmann, S. Vogt, J. Maser, C. L. Harland, E. Van Achterbergh, D. Legnini, *Nucl. Instruments Methods Phys. Res. Sect. B Beam Interact. with Mater. Atoms* **2005**, *231*, 183.
[155] T. Schoonjans, V. A. Solé, L. Vincze, M. Sanchez Del Rio, K. Appel, C. Ferrero, *Spectrochim. Acta - Part B At. Spectrosc.* **2013**, *82*, 36.
[156] V. A. Solé, E. Papillon, M. Cotte, P. Walter, J. Susini, *Spectrochim. Acta - Part B At. Spectrosc.* **2007**, *62*, 63.
[157] S. Vogt, *J. Chem. Inf. Model.* **2003**, *104*, 635.
[158] S. Vogt, M. De Jonge, B. Lai, J. Maser, Manual for the MAPS software package. *Argonne Natl. Lab.* **2006**, 1–5.
[159] T. Nietzold, B. M. West, M. Stuckelberger, B. Lai, S. Vogt, M. I. Bertoni, *J. Vis. Exp* **2018**, *In-press*.
[160] H. Hieslmair, A. A. Istratov, R. Sachdeva, E. . Weber, *Cryst. Silicon Sol. Cell Mater. Process* **2000**, *33*, 162.
[161] O. F. Vyvenko, T. Buonassisi, A. A. Istratov, H. Hieslmair, A. C. Thompson, R. Schindler, E. R. Weber, *J. Appl. Phys.* **2002**, *91*, 3614.
[162] G. Martínez-Criado, B. Alen, A. Homs, A. Somogyi, C. Miskys, J. Susini, J. Pereira-Lachataignerais, J. Martínez-Pastor, *Appl. Phys. Lett.* **2006**, *89*, 221913.
[163] C. A. Klein, *J. Appl. Phys.* **1968**, *39*, 2029.
[164] A. E. Morishige, H. S. Laine, E. E. Looney, M. A. Jensen, S. Vogt, J. B. Li, B. Lai, H. Savin, T. Buonassisi, *IEEE J. Photovoltaics* **2017**, *7*, 763.
[165] T. J. Jacobsson, J. P. Correa-Baena, E. Halvani Anaraki, B. Philippe, S. D. Stranks, M. E. F. Bouduban, W. Tress, K. Schenk, J. Teuscher, J. E. Moser, H. Rensmo, A. Hagfeldt, *J. Am. Chem. Soc.* **2016**, *138*, 10331.
[166] G. E. Eperon, S. N. Habisreutinger, T. Leijtens, B. J. Bruijnaers, J. J. Van Franeker, D. W. Dequilettes, S. Pathak, R. J. Sutton, G. Grancini, D. S. Ginger, R. A. J. Janssen, A. Petrozza, H. J. Snaith, *ACS Nano* **2015**, *9*, 9380.
[167] I. C. Smith, E. T. Hoke, D. Solis-Ibarra, M. D. McGehee, H. I. Karunadasa, *Angew. Chemie* **2014**, *126*, 11414.
[168] S. Aharon, B. El Cohen, L. Etgar, *J. Phys. Chem. C* **2014**, *118*, 17160.
[169] K. X. Steirer, P. Schulz, G. Teeter, V. Stevanovic, M. Yang, K. Zhu, J. J. Berry, *ACS Energy Lett.* **2016**, *1*, 360.
[170] Y. Luo, P. Khoram, S. Brittman, Z. Zhu, B. Lai, S. P. Ong, E. C. Garnett, D. P. Fenning, *Adv. Mater.* **2017**, 1.
[171] A. Dualeh, T. Moehl, N. Tetreault, J. Teuscher, P. Gao, M. K. Nazeeruddin, M. Gratzel, *ACS Nano* **2014**, *8*, 362.

[172] T. Y. Yang, G. Gregori, N. Pellet, M. Grtäzel, J. Maier, *Angew. Chemie - Int. Ed.* **2015**, *54*, 7905.
[173] D. W. deQuilettes, W. Zhang, V. M. Burlakov, D. J. Graham, T. Leijtens, A. Osherov, V. Bulović, H. J. Snaith, D. S. Ginger, S. D. Stranks, *Nat. Commun.* **2016**, *7*, 1.
[174] J. M. Frost, A. Walsh, *Acc. Chem. Res.* **2016**, *49*, 528.
[175] J. Emara, T. Schnier, N. Pourdavoud, T. Riedl, K. Meerholz, S. Olthof, *Adv. Mater.* **2016**, *28*, 553.
[176] W. Tress, N. Marinova, T. Moehl, S. M. Zakeeruddin, M. K. Nazeeruddin, M. Grätzel, *Energy Environ. Sci.* **2015**, *8*, 995.
[177] J. Beilsten-Edmands, G. E. Eperon, R. D. Johnson, H. J. Snaith, P. G. Radaelli, *Appl. Phys. Lett.* **2015**, *106*, 173502.
[178] Y. Yuan, J. Chae, Y. Shao, Q. Wang, Z. Xiao, A. Centrone, J. Huang, *Adv. Energy Mater.* **2015**, *5*, 1.
[179] Y. Yuan, J. Huang, *Acc. Chem. Res.* **2016**, 286.
[180] P. Khoram, S. Brittman, W. I. Dzik, J. N. H. Reek, E. C. Garnett, *J. Phys. Chem. C* **2016**, *120*, 6475.
[181] Y. Tidhar, E. Edri, H. Weissman, D. Zohar, D. Cahen, B. Rybtchinski, S. Kirmayer, *J. Am. Chem. Soc.* **2014**, *136*, 13249.
[182] D. E. Starr, G. Sadoughi, E. Handick, R. G. Wilks, J. H. Alsmeier, L. Kö, M. Gorgoi, H. J. Snaith, M. Bä, *Energy Environ. Sci.* **2015**, *8*, 1609.
[183] W. Rehman, R. L. Milot, G. E. Eperon, C. Wehrenfennig, J. L. Boland, H. J. Snaith, M. B. Johnston, L. M. Herz, *Adv. Mater.* **2015**, *27*, 7938.
[184] A. Sadhanala, F. Deschler, T. H. Thomas, S. E. Dutton, K. C. Goedel, F. C. Hanusch, M. L. Lai, U. Steiner, T. Bein, P. Docampo, D. Cahen, R. H. Friend, *J. Phys. Chem. Lett.* **2014**, 2501.
[185] D. P. Mcmeekin, G. Sadoughi, W. Rehman, G. E. Eperon, M. Saliba, M. T. Hörantner, A. Haghighirad, N. Sakai, L. Korte, B. Rech, M. B. Johnston, L. M. Herz, H. J. Snaith, M. T. Horantner, A. Haghighirad, N. Sakai, L. Korte, B. Rech, M. B. Johnston, L. M. Herz, H. J. Snaith, *Science* **2016**, *351*, 151.
[186] S. Van Reenen, M. Kemerink, H. J. Snaith, *J. Phys. Chem. Lett.* **2015**, *6*, 3808.
[187] E. L. Unger, E. T. Hoke, C. D. Bailie, W. H. Nguyen, A. R. Bowring, T. Heumüller, M. G. Christoforo, M. D. McGehee, *Energy Environ. Sci.* **2014**, *7*, 3690.
[188] S. J. Yoon, S. Draguta, J. S. Manser, O. Sharia, W. F. Schneider, M. Kuno, P. V. Kamat, *ACS Energy Lett.* **2016**, *1*, 290.
[189] P. Gratia, G. Grancini, J. Audinot, X. Jeanbourquin, E. Mosconi, I. Zimmermann, D. Dowsett, Y. Lee, M. Gra, F. De Angelis, *J. Am. Chem. Soc.* **2016**, *138*, 15821.
[190] J. L. Luria, N. Hoepker, R. Bruce, A. R. Jacobs, C. Groves, J. a Marohn, *ACS Nano* **2012**, *6*, 9392.
[191] B. Philippe, M. Saliba, J. P. Correa-Baena, U. B. Cappel, S. H. Turren-Cruz, M. Grätzel, A. Hagfeldt, H. Rensmo, *Chem. Mater.* **2017**, *29*, 3589.
[192] Z. Guo, S. J. Yoon, J. S. Manser, P. V. Kamat, T. Luo, *J. Phys. Chem. C* **2016**, *120*, 6394.
[193] M. T. Klug, A. Osherov, A. A. Haghighirad, S. D. Stranks, P. R. Brown, S. Bai, J. T.-W. Wang, X. Dang, V. Bulović, H. J. Snaith, A. M. Belcher, *Energy Environ. Sci.* **2017**, *10*, 236.
[194] J. T.-W. Wang, Z. Wang, S. Pathak, W. Zhang, D. W. DeQuilettes, F. Wisnivesky-Rocca-Rivarola, J. Huang, P. K. Nayak, J. B. Patel, H. A. M. Yusof, Y. Vaynzof, R. Zhu, I. Ramirez, J. Zhang, C. Ducati, C. Grovenor, M. B. Johnston, D. S. Ginger, R. J. Nicholas, H. J. Snaith, *Energy Environ. Sci.* **2016**, 2892.
[195] J. R. Poindexter, R. L. Z. Hoye, L. Nienhaus, R. C. Kurchin, A. E. Morishige, E. E. Looney, A. Osherov, B. Lai, V. Bulovic, V. Stevanovic, M. G. Bawendi, T. Buonassisi,

*ACS Nano* **2017**, In press.
[196] S. Zou, Y. Liu, J. Li, C. Liu, R. Feng, F. Jiang, Y. Li, J. Song, H. Zeng, M. Hong, X. Chen, *J. Am. Chem. Soc* **2017**, *139*, 11443.
[197] M. D. Sampson, J. S. Park, R. D. Schaller, M. K. Y. Chan, A. B. F. Martinson, *J. Mater. Chem. A* **2017**, *5*, 3578.

# The Relationship Between Chemical Flexibility and Nanoscale Charge Collection in Hybrid Halide Perovskites

*Yanqi Luo,[1] Sigalit Aharon,[2] Michael Stuckelberger,[3] Ernesto Magana,[1] Barry Lai,[4] Mariana I. Bertoni,[3] Lioz Etgar,[2] and David P. Fenning*[*,1]*

**Keyword:** Hybrid perovskite, nanoscale characterization, mixed halide, x-ray fluorescence, x-ray beam induced current, solar cell

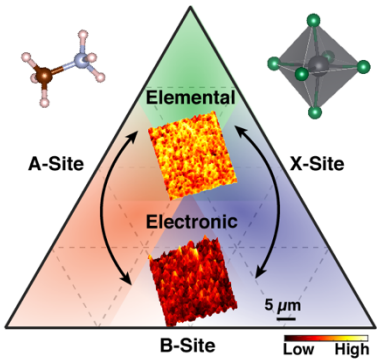


**Hybrid** halide perovskite thin films exhibit complex chemistry at the nanoscale that can affect their optoelectronic performance. *in-situ* characterization of chemistry and functionality, such as by *operando* X-ray fluorescence and X-ray beam induced current measurements of perovskite solar cells, reveals insights into the relationship between local current collection, non-stoichiometry, and chemistry composition in hybrid lead perovskite absorbers.